Università degli Studi di Firenze
Scuola di Ingegneria
DIEF - Department of Industrial Engineering of Florence

PhD School: *Energetica e Tecnologie Industriali ed Ambientali Innovative*
Scientific Area: ING-IND/08 - *Macchine a Fluido*

Design tools and innovative concepts for gas turbine cooling applications

PhD Candidate: Ing. Lorenzo Winchler

Tutor: Prof. Ing. Bruno Facchini

Academic Supervisor: Dr. Ing. Antonio Andreini

Industrial Supervisor: Dr. Ing. Luca Innocenti

PhD School Coordinator: Prof. Ing. Maurizio De Lucia

XXVIII PhD School Cycle - 2013-2015

To my beloved grandparents,
whose affection helped me become the man I am today.

Acknowledgements

Desidero ringraziare prima di tutti il Prof. Bruno Facchini per avermi dato la possibilità di crescere professionalmente e come persona offrendomi un posto nel suo gruppo, nonostante provenissi da un differente percorso di studi: sentire la sua fiducia è stato fondamentale, soprattutto nei primi mesi. Vorrei poi ringraziare il coordinatore del dottorato, prof. Maurizio De Lucia, per i suoi consigli e per avermi sempre aiutato con gli intoppi burocratici.

Grazie inoltre al (neo) professor Carlo Carcasci per avermi iniziato al Fortran ed ai linguaggi di programmazione, e per avermi sempre mostrato disponibilità, rispetto e fiducia: grazie per aver sempre lasciato la porta aperta per me. Non sarei riuscito però a fare nemmeno metà del mio percorso senza l'aiuto e il tempo che mi ha dedicato l'Ing. Antonio Andreini: la sua dedizione al lavoro, la sua conoscenza scientifica e tecnica e l'immensa pazienza e disponibilità che mi ha offerto, sono stati infatti fondamentali nella mia crescita e per completare questo lavoro.

Desidero poi ringraziare tutte le persone che lavorano in GE Oil & Gas Nuovo Pignone® come Alberto Ceccherini, Francesco Maiuolo, Gianluca Caciolli e soprattutto Alessio Bonini, con il quale ho condiviso gioie e dolori per almeno due terzi del mio ciclo di dottorato, e che mi ha insegnato davvero tanto. Grazie anche al mio tutor industriale Ing. Luca Innocenti, per avermi supervisionato e per aver sempre trovato un po' del suo poco tempo da dedicarmi.

Grazie anche a tutti i ragazzi di Ergon Research (Lorenzo, Riccardo, Cosimo e Mirko) e infine a tutti i miei colleghi con i quali ho condiviso

pranzi, rinfreschi, conferenze, lezioni, seminari e soprattutto tante tante ore insieme: tutti i *lab guys*, Daniele, Riccardo, Tommaso, con un ringraziamento particolare a chi mi ha aiutato con le prove sperimentali presenti in questa tesi, Giulio, Alessio e Lorenzo, e tutti i *numerici*, Stefano, Davide, Daniele, Leopoldo, Sabrina, Emanuele, Alessandro e Tommaso (le scene a Quebec City rimarranno per sempre nella storia). Un ringraziamento speciale a Lucuccio e a Lorenzuccio, che mi hanno insegnato davvero tanto, con i quali è stato un piacere lavorare insieme e che sono felice siano diventati miei amici.

Grazie a tutti i miei amici, alla mia fantastica famiglia che mi ha sempre supportato e soprattutto ai miei genitori, ai quali va la mia infinita gratitudine per i sacrifici ed il supporto costante che mi hanno mostrato fin dal primo giorno di università.

Un immenso grazie va infine alla mia splendida Giulia, per la pazienza, per il supporto, per essere stata convinta delle mie potenzialità più di quanto lo fossi io, per essermi rimasta accanto nei momenti di difficoltà, per aver rinunciato a molti weekend e giorni festivi per lasciarmi studiare e lavorare, per aver condiviso con me le gioie della convivenza... per avermi completato.

"If I have seen further
it is by standing on the shoulders of giants."
Isaac Newton, 1676

Abstract

The improvement in thermal efficiency and specific power output in gas turbine engines depends on the possibility of increasing Turbine Inlet Temperature (TIT). This has become during the last years one of the main target in engine development, and nowadays TIT can overtake higher values than those allowed by material's resistance. Despite the constant development concerning materials, it is possible to raise engine operating temperature only by cooling gas turbine components, ensuring them an adequate lifetime. Since cooling system use air bled from the compressor, it has a cost on the performance of thermodynamic cycle: a progressive reduction of the global efficiency inevitably occurs increasing the amount of coolant. Gas turbine designers have the goal to maximize cooling system effectiveness, or in other terms ensure required component lifespan using a minimal amount of coolant flow. To this purpose, it is necessary to develop tools able to accurately and quickly estimate thermal loads and predict metal temperature on gas turbine components. Three inherently linked heat transfer problems have to be solved for estimating metal temperature in a GT component: external convection performed by hot gas coming from the combustion chamber, internal convection achieved from coolant flow, and conduction within the metal component.

It is here proposed a numerical procedure, developed in collaboration with *GE Oil&Gas Nuovo Pignone*® , aimed to perform Conjugate Heat Transfer (CHT) calculations of cooled vanes and blades, where the internal cooling system is modeled by a one dimensional thermo-fluid network solver mainly based on heat transfer and pressure losses correlations

coming from the open literature. Thermal loads and pressure distributions on the external profile are obtained by 3D CFD analysis, while heat conduction in the solid is estimated by a 3D FEM solver, which uses data computed by 3D CFD and fluid network solver as boundary conditions. The great advantage of this procedure is represented by the possibility to speed up the design phase respect to a complete CHT calculation, since CFD and FEM calculations are performed without discretization of cooling holes, using correlative and lower order methodologies, and since the solution of internal cooling system is performed by a fluid network solver, decoupled from other domains. This allows to decrease computational time and permits a faster analysis without renouncing to an adequate overall accuracy, assuring feasibility in both preliminary and detailed design phases. In order to validate the proposed methodology, the procedure was applied to two different test cases, which represent two gas turbine blades with different cooling configuration.

Numerical tools involved in the procedure are then used for the design of two different innovative gas turbine cooling systems: one based on impingement and the other on film cooling. Theses concepts are designed by thinking of a production via additive manufacturing, where limits imposed by casting and chip removal machining can be overcome. CFD analyses and experimental activities are carried out in order to improve the innovative concepts' performance and validate the numerical methodology, recognizing its capabilities as a fast design tool for both existent and innovative cooling systems.

Contents

Nomenclature

Acronyms

API	Application Programming Interface
$BANKS$	Blades And Nozzles networK Solver
$BLANK CODE$	BLades And Nozzles networK COnjugate DEsign
BEM	Boundary Element Method
CAD	Computer Aided Design
CCT	Conjugate Calculation Technique
CFD	Computational Fluid Dynamics
CHT	Conjugate Heat Transfer
CT	Computed Tomography
$DMLS$	Direct Metal Laser Sintering
DoE	Design of Experiments
DP	Design Point
EDM	Electrical Discharge Machining
FC	Film Cooling
FEM	Finite Element Method
FVM	Finite Volume Method
GT	Gas Turbine
$HPHT$	High Pressure High Temperature
LE	Leading Edge
LHS	Latin Hypercube Sampling
$MOGA$	Multi Objective Genetic Algorithm

$NEST$	NEtwork Setup Tool
NGV	Nozzle Guide Vane
OSF	Optimal Space Filling
PS	Pressure side
PSP	Pressure Sensitivity Paint
$RANS$	Reynolds-Averaged Navier-Stokes equations
SS	Suction Side
SST	Shear Stress Transport
TBC	Thernal Barrier Coating
TE	Trailing Edge
TET	Turbine Entry Temperature
TIT	Turbine Inlet Temperature
TPF	Thermal Performance Factor

Greeks

α	First innovative film cooling angle	$[^\circ]$
β	Second innovative film cooling angle	$[^\circ]$
β	Pressure Ratio	$[-]$
γ	Heat capacity ratio	$[-]$
γ	Intermittency	$[-]$
γ	Trapezoid angle	$[^\circ]$
δ	Manufacturing angle	$[^\circ]$
ϵ	$R/c_p = (\gamma - 1)/\gamma$	$[-]$
$\bar{\eta}$	Averaged adiabatic effectiveness	$[-]$
$\eta,\ \eta_{ad},\ \eta_{aw}$	Adiabatic effectiveness	$[-]$
η_c	Compressor efficiency	$[-]$
η_r	Real efficiency	$[-]$
η_t	Turbine efficiency	$[-]$
Θ	Dimensionless temperature	$[-]$
μ	Dynamic viscosity	$[Pa\ s]$
ξ	Non-dimensional parameter	$[-]$
ρ	Density	$[kg\ m^{-3}]$

τ	Maximum over inlet T ratio	$[-]$
φ	Cooling effectiveness	$[-]$
ω	Turbulence frequency	$[s^{-1}]$

Letters

A	Constant or parameter	$[-]$
A	Area	$[m^2]$
Ax_{Ch}	Axial chord	$[m]$
AR	Area Ratio	$[-]$
B	Constant or parameter	$[-]$
BR	Blowing Ratio	$[-]$
C, C_1, C_2, C_3	Constant	$[-]$
C_d, C_D	Coefficient of Discharge	$[-]$
C_{gas}	Oxygen concentration in free stream	$[-]$
C_w	Oxygen concentration near the wall	$[-]$
c_p	Specific heat at constant pressure	$[J\ kg^{-1}\ K^{-1}]$
D	Diameter	$[m]$
DR	Density Ratio	$[-]$
f	Friction factor	$[-]$
G_c	Crossflow mass flux	$[kg\ s^{-1}\ m^{-2}]$
G_j	Jet mass flux	$[kg\ s^{-1}\ m^{-2}]$
HTC	Heat transfer coefficient	$[W\ m^{-2}\ K^{-1}]$
I	Momentum flux ratio	$[-]$
k	Turbulent kinetic energy	$[m^2\ s^{-2}]$
k	Thermal conductivity	$[W\ m^{-1}\ K^{-1}]$
L	Total length	$[m]$
L_d	Turbulent length scale	$[m]$
Le	Lewis number	$[-]$
Ma	Mach number	$[-]$
$\dot{m}$	Mass flow rate	$[kg\ s^{-1}]$
m	Constant or correlation parameter	$[-]$
$NHFR$	Net Heat Flux Reduction	$[-]$
Nu	Nusselt number	$[-]$

$n,\ n_x,\ n_y,\ n_z$	Constant or correlation parameter	$[-]$
P	Pressure	$[Pa]$
P	Pitch	$[m]$
$P0$	Total Pressure	$[Pa]$
Pr	Prandtl number	$[-]$
Q	Thermal power	$[W]$
q_{joule}	Joule heating power	$[W]$
$\dot{q}$	Heat flux	$[W\ m^{-2}]$
R	Gas constant	$[J\ kg^{-1}\ K^{-1}]$
Re	Reynolds number	$[-]$
Re_θ	Momentum thickness Re number	$[-]$
S	Curvilinear abscissa	$[m]$
S_{tot}	Total curvilinear length	$[m]$
T	Temperature	$[K]$
$T0$	Total Temperature	$[K]$
TR	Temperature ratio	$[-]$
Tu	Turbulence intensity	$[-]$
t	Plate thickness	$[m]$
t	Trapezoid maximum base	$[m]$
$V,\ v$	Velocity magnitude	$[m\ s^{-1}]$
VR	Velocity ratio	$[-]$
$X,\ x,\ Y,\ y,\ Z,\ z$	Generic directions or pitch	$[m]$
y^+	Dimensionless wall distance	$[-]$

Subscripts

ad	Adiabatic
ave	Average
aw	Adiabatic wall
b	Blade
c	Coolant
$exit$	Film cooling outlet
ext	External
fix	Fixed

g	Gas
i	Generic coefficient
in	Inlet
int	Internal
iso	Isentropic
m	Mainstream
nom	Nominal
out	Outlet
ref	Reference
s	Static
w	Wall
0	Reference
0	Total quantity
0	Without film cooling

Superscripts

eq	Equivalent

Introduction

Thermodynamic cycle used by gas turbine engines is Brayton cycle and it's well known that a direct method to increase cycle efficiency is to raise the engine pressure ratio or to raise the maximum cycle temperature [1], as we can see in Eq. 1, where real efficiency of gas turbine engine and its dependence from temperature ratio τ is shown, as reported in [2].

$$\eta_r = \frac{1-\beta^{-\epsilon}}{\eta_c}\left[\frac{1-(1-\eta_c\,\eta_t)}{1-\beta^{\epsilon}/\tau}\right] \tag{1}$$

Looking at Eq. 1, where β is gas turbine pressure ratio and η_c and η_t are compressor and turbine efficiency respectively, it's possible to notice that an increase of η_r, while component efficiencies and pressure ratio are fixed, it's possible just by increasing temperature ratio τ and so the maximum cycle temperature; these dependencies can be appreciated in Figure 1, where η_r is plotted for different τ respect to β values.

For that reason, over the past decades, gas turbine designers have endeavored to increase the temperature exiting from the combustion chamber, called Turbine Entry Temperature (TET) or Turbine Inlet Temperature (TIT). The effort is justified by a significant performance increase, as depicted in Figure 2 and expected by the theoretical formulation of power, represented as the full line called "Ideal performance" in the above cited figure.

Obviously the increase in temperature is directly linked with a decrease in strength of components exposed to TET; specific manufacturing techniques, like directionally-solidification and single-crystal castings, were

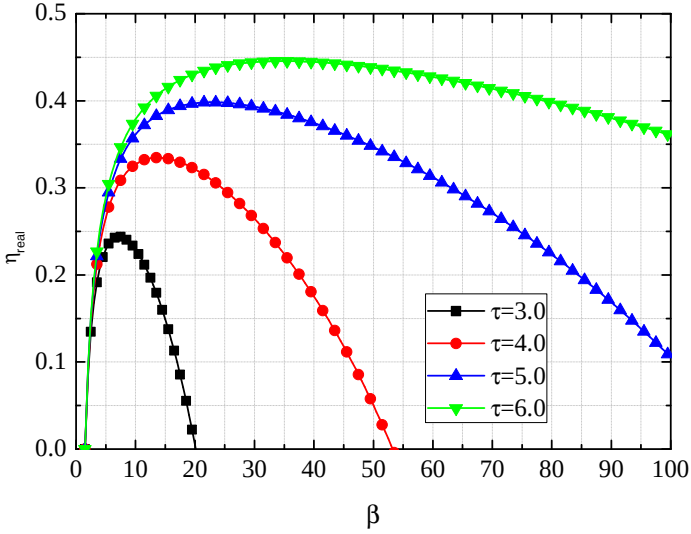

Figure 1: Gas turbine real efficiency respect to β for different τ. $\eta_c = 0.88$, $\eta_t = 0.90$.

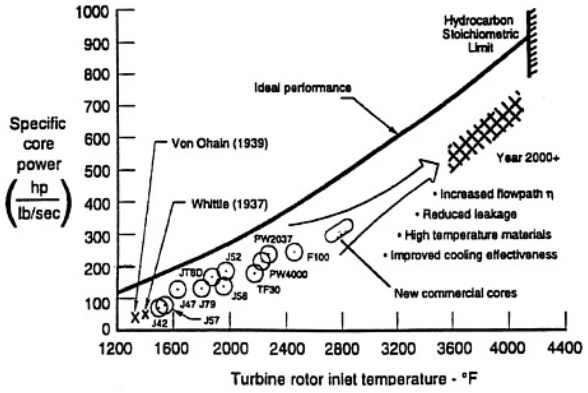

Figure 2: Power increase enabled by TET increase [3].

developed appositely for increasing gas turbines parts' life and nowadays many airfoils use single crystal super-alloys guaranteeing satisfying thermo-physical properties [4, 5, 6, 7, 8]. These two-phase alloys are mainly composed of nickel (Ni), with smaller weight percent of various other elements in solid solution [9] like cobalt (Co), aluminum (Al), chromium (Cr), tungsten (W), molybdenum (Mo), tantalum (Ta), hafnium (Hf), rhenium (Re), and ruthenium (Ru) [10]. Despite all the efforts performed by material's designers, it would not be possible to reach TET values of 1800-1900 K without the presence of an accurate cooling system. Most of the recent improvements come from a greater understanding of the heat transfer and the three-dimensional temperature distribution in the turbine passage. In Figure 3 it can be appreciated how the contemporary development of new materials and cooling techniques had allowed to reach TET values higher than metal melting temperature.

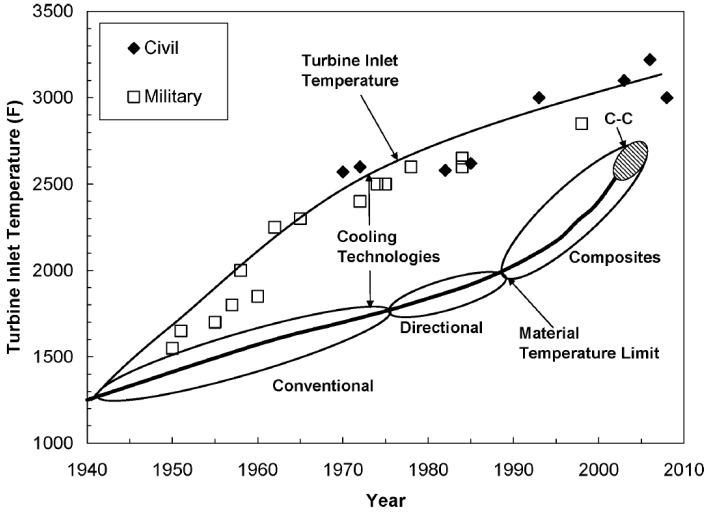

Figure 3: Comparison between TIT and blade material temperature limits highlighting the importance of cooling technology, [11].

Only by using non metallic materials, like ceramic or composite, or applying a Thermal Barrier Coating (TBC) it's possible to reach even higher temperature values. As stated by Bunker [12], the conventional cooling technology applied on gas turbines consists of five main elements: internal convective cooling, external surface film cooling, materials selection, thermo-mechanical design at both component and system levels, selection pretreatment of the coolant fluid. These aspects define the thermal management capabilities and limitations in modern gas turbines that nowadays can reach very advanced requirements. Any further increases in efficiency and lifespan may be obtained by small incremental improvements or by completely changing cooling systems' manufacturing process, for example by the use of *additive manufacturing* techniques like DMLS (Direct Metal Laser Sintering). 3D printing allows to realize detailed prototypes and even final components for experimental activities, increasing accuracy and representativeness of tests, also because the powder used in DMLS can be of the same materials used for gas turbine components like titanium, or super-alloys of nichel and cobalt. Additive manufacturing open new roads for gas turbine cooling, allowing to realize the component and its cooling system at the same time.

Considering that even small variation of blade temperature leads to a strong reduction of its lifespan, fast and reliable techniques aimed at predicting heat loads and temperature distributions on a gas turbine component appear to be mandatory in its design process.

Research objectives

This work presents a Conjugate Heat Transfer (CHT) procedure, developed in collaboration with *GE Oil&Gas Nuovo Pignone*® , aimed at predicting metal temperatures on gas turbine nozzles and blades, based on a modular and correlative approach. This procedure, that is an improvement of the one described in [13] and [14], has been used as a design tool for two innovative cooling techniques for gas turbine nozzles and blades: the first based on an internal cooling technique and the second

on blade protection. Both components are designed for being applied on a first or second vane's nozzle or blade realized with DMLS: by doing this, the cooling system of the vane can be manufactured together with the airfoil, given the possibility to realize much more complicated geometries, overcoming the limits imposed by casting and subtractive manufacturing. Objectives of this work is to validate the presented procedure on different cases and to use it as a tool for a fast design of gas turbine cooling innovative components, showing its modularity and flexibility. The use of DLMS technique together with a fast procedure for temperature evaluation can speed up the entire design phase of gas turbine components, allowing to rapidly test different innovative geometries.

Thesis outline

The present thesis is structured as follows.

Chapter 1 presents gas turbine cooling techniques. Main features of cooling systems are presented, giving both a theoretical background and a literature review, focusing on *impingement* and *film cooling* systems.

Chapter 2 reports a description of the proposed conjugate heat transfer methodology for predicting gas turbine components' temperature. In the second part of the chapter the procedure is then validated by using two different experimental test case, well described in literature.

Chapter 3 focuses on the description of an innovative concept of impingement cooling, having the goal to lower the detrimental effect of crossflow in large array with dozens of holes, like in a gas turbine endwall or in a second stage's vane. The concept geometry is simulated via 3D CHT CFD simulations and improved by using the presented procedure. The innovative configuration is then applied to a simulated real engine second stage's vane and compared to a standard impingement geometry. An experimental test plate is than designed with the procedure and realized; finally a comparison with the experimental data is shown.

Chapter 4 reports a description of an innovative film cooling shaped hole. Geometry is optimized by using a genetic algorithm linked to a CFD solver, and the more promising geometry is then 3D printed and tested by using pressure sensitive paint. Experimental results are then compared with the ones given by a typical correlation developed for shaped holes.

Chapter 1

Gas turbine cooling

This chapter describes most used cooling and protection systems in gas turbine cooling and their characterization through correlations. Main goal of cooling systems is to maintain gas-path components to temperatures several hundred degrees below gas temperature T_g, in order to allow continued operation of these components without failure: as a matter of fact high metal temperatures lead to high component thermal stresses and hence to failures. Typically, cooling is provided by extracting some compressed air and bypassing the combustion chamber directly into the turbine. Extraction of the working fluid imposes a penalty to system efficiency, as work has been done on the fluid to compress it. Also, addition of coolant back into the hot gas stream imposes further thermodynamic penalties. First developed and most common techniques are internal convection cooling, like impingement, turbulated multi-pass serpentine passages, flow through pin-fin arrays or simply smooth or turbulated radial channels. External methods allows coolant from inside the blade to eject out onto the hot-gas side surface through discrete holes, creating a small layer that protect the blade. This method is called film cooling.

An important parameter for analyzing internal gas turbine cooling performances is *cooling effectiveness* φ, a dimensionless temperature ratio of gas to metal over gas to internal coolant temperature difference [15]:

$$\varphi = \frac{T_g - T_b}{T_g - T_c} \tag{1.1}$$

If the cooling effectiveness is non-existent, or zero, there is no cooling effect; whereas, if it's equal to unity, airfoil metal and coolant temperature are the same. φ characterizes the cooling circuit performance inside the turbine airfoil and typical values of different systems are reported in Figure 1.1.

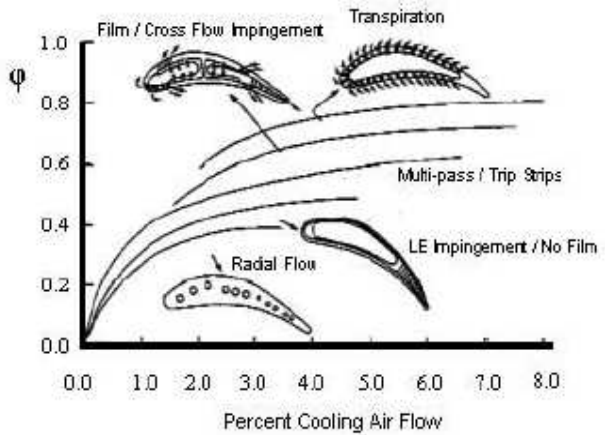

Figure 1.1: Cooling effectiveness for different cooling schemes, [1].

As illustrated in Figure 1.1, cooling effectiveness increases rapidly with small amounts of coolant at lower rate, but if we want to increase φ over a certain value it's possible only by requiring a large amount of coolant or by changing cooling system.

From the first radially cooled blade developed in the 40's to complex multi-pass systems available in current blades, many improvements has been performed during the years (Fig. 3), but in all cases heat transfer phenomena involved can be described by Newton's equation (1.2). Total heat removed can be expressed multiplying Newton's equation for total

surface exposed to heat transfer A (1.3): increasing this value can be a good method for increasing heat removal in gas turbine components, for example in multi-pass configuration.

$$\dot{q} = HTC\,(T_{ref} - T_w) \tag{1.2}$$

$$Q = \dot{q}\,A = HTC\,A\,(T_{ref} - T_w) \tag{1.3}$$

In Newton's equation $\dot{q}$ is the heat flux, while the proportional coefficient HTC represents the heat transfer coefficient, which is a complex function of geometry, fluid dynamic conditions, fluid properties and even temperature difference. Reference temperature in Equation 1.2 for gas turbine applications can be adiabatic wall temperature T_{aw}, that is the one acquired by a wall in liquid or gaseous flow if the condition of thermal insulation (heat flux equal zero) is observed on it. So Equation 1.2 becomes:

$$\dot{q} = HTC\,(T_{aw} - T_w) \tag{1.4}$$

HTC value is hard to be determined analytically, but different method can be used, such as the mass-transfer analogy or experimental activities combined with dimensional analysis by using Buckingham's theorem [16]. For example analyzing the problem of correlating experimental data for convective forced heat transfer of air flowing inside a heated pipe, 7 physical variables are present $(D, k, V, \rho, \mu, c_p, HTC)$ and 4 elementary dimensions (kg, m, K, s): Buckingham's theorem stated that only $7 - 4 = 3$ non dimensional numbers can be used for describing the problem. After some calculations reported in [16], the link among the three non dimensional groups, described below, is reported in 1.5.

$$Nu = f(Re, Pr) \tag{1.5}$$

$$Nu = \frac{HTC\,D}{k} \quad (1.6) \qquad Re = \frac{\rho\,V\,D}{\mu} \quad (1.7) \qquad Pr = \frac{\mu\,c_p}{k} \quad (1.8)$$

Heat transfer coefficient can be evaluated knowing Nusselt number (Eq. 1.6) when the correlation between Reynolds number Re and Prandtl number Pr is known; a large set of heat transfer correlation are based on Re and Pr dependencies. It's also fundamental to check the impact on friction factor when developing methods for increasing heat transfer performances: for that reason experimental and numerical results related to gas turbine cooling component's performance are often reported in terms of Thermal Performance Factors (TPFs) (1.9, 1.10). TPF_1 can be used for comparing different cooling methods respect to a reference case, while TPF_2 can be a good parameter for comparing performances inside a channel, considering same mass flow and same pumping power [17].

$$TPF_1 = \left(\frac{Nu}{Nu_0}\right) \Big/ \left(\frac{f}{f_0}\right) \quad (1.9)$$

$$TPF_2 = \left(\frac{Nu}{Nu_0}\right) \Big/ \left(\frac{f}{f_0}\right)^{1/3} \quad (1.10)$$

Now a review of the main cooling techniques and performance correlations are presented, with a particular attention on impingement and film cooling.

1.1 Radial and multi-pass ducts

Main basic cooling system is represented by radial ducts. Radial ducts are a series of smooth channels where the coolant flow enters from the hub of the blade, and sometimes also from the tip, and develops along the radial direction. To increase heat transfer coefficient, turbulence value or total surface cooled by the flow can be increased; in Figure 1.2 different radial cooling solution are shown: HTC is increased going from a single pass to a multi-pass configuration, where total surface is widely increase.

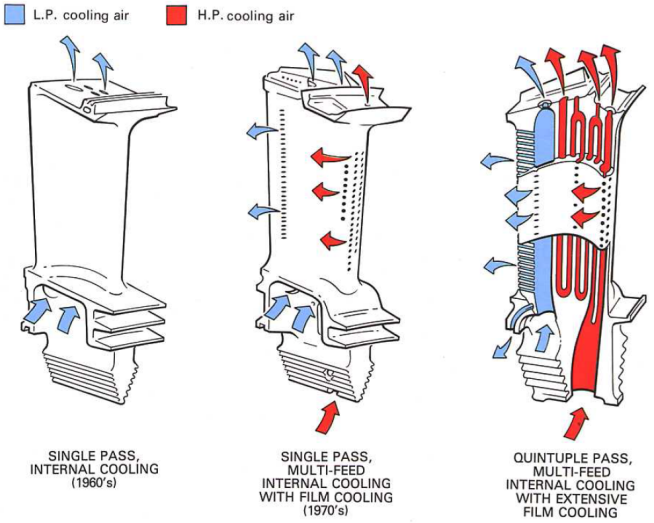

Figure 1.2: Radial single and multi-pass cooling channels, [18].

Turbulence value can be increased by adding non-aerodynamics objects (like rectangular *ribs*) inside ducts: they act like turbulence promoters by interrupting boundary layer. After boundary layer is disturbed, re-development begins, and high heat transfer is associated with the thin boundary layer. Figure 1.3 presents conceptual views of the most notable characteristics of the effects of ribs on the mainstream flow. As shown in Figure 1.3, as the mainstream flow near the surface of the channel passes over the rib, it separates from the surface. This separation results in relatively low heat transfer just downstream of the rib, due to a relatively hot cell being trapped in the area of recirculation. However, when the mainstream flow reattaches to the surface (between two ribs), this is an area of relatively high heat transfer due to the impingement of the mainstream flow on the surface. This pattern of separation, recirculation, and reattachment continues throughout the channel along with the pattern of repeating ribs [19, 20].

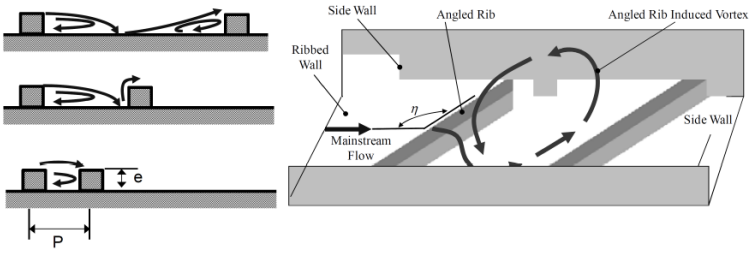

Figure 1.3: Rib effects on mainstream and secondary flows, [20].

Many heat transfer and pressure losses correlations are available in literature for radial ducts, both in smooth and turbulated configurations. Most used smooth channel's heat transfer correlations are developed by Colburn, Nusselt, Dittus Boelter, Gnielinski [21], while main pressure losses correlation can be found in [22]. Many correlations are available for characterizing ribbed ducts: most important can be found in [17].

1.2 Pin-fins

Pin-fins are prismatic support, generally having circular cross sections, widely used in gas turbine trailing edge cooling. They are placed orthogonally to the flow direction to maximize forced convection cooling; the main advantage consists in increasing heat transfer coefficient without increasing the thickness of airfoil blade. Flow around the pin fin behaves in the same way as around a single cylinder: the coolant separates and wakes are shed downstream, whereas a horseshoe vortex forms upstream of the base of the pin, wrapping it and creating additional mixing. In addition to flow disturbances, pins conduct thermal energy away from the heat transfer surface, and long pins can increase the effective heat transfer area. Pin spacing (in both streamwise and spanwise direction), size, shape, or fillet radii dimensions, are all factors that can influence heat transfer performance.

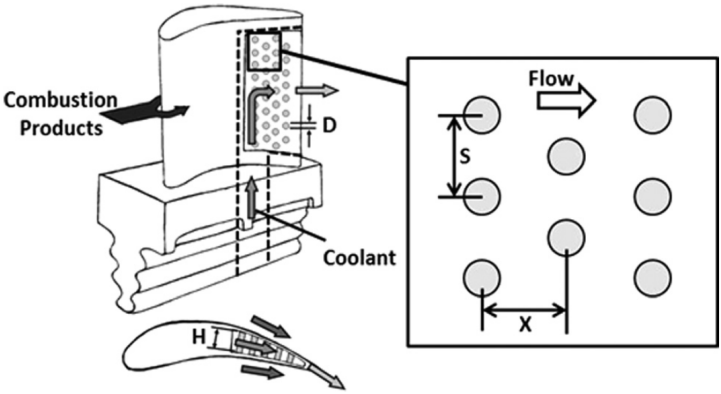

Figure 1.4: Schematic of a pin-fin array at the trailing edge of a gas turbine airfoil, [23].

Most important correlations for pin-fin cooling are developed by VanFossen [24] and Metzger et al. [25] for short pin-fin arrays (height over diameter < 3), and by Faulkner [26] for tall pin-fin arrays (height over diameter > 3), as stated by Armstrong and Winstanley [27] in their review.

1.3 Dimples

Dimples are arrays of indentations along internal surfaces. These are most commonly spherical in shape, although a variety of other shapes have also been employed, including triangular and tear-drop. Arrays of dimples are beneficial method for internal cooling because they produce multiple vortex pairs which augment local Nusselt number distributions as they advect downstream. They are notable for the low pressure drop penalties which they produce, which is because they do not protrude into the flow to produce significant amounts of form drag. With this benefit, dimples offer advantages for cooling later turbine stages where lower pressure

cooling air is employed. They are also advantageous because the pressure drop that they produce through an airfoil passage is relatively low, which allows favorable pressure margins to be maintained in parts of the airfoil interior which are further downstream [28, 29]. Another benefit is dimple manufacture removes material from internal cooling passage components, in contrast to rib turbulators and pin fins, which require addition of extra material and weight [28].

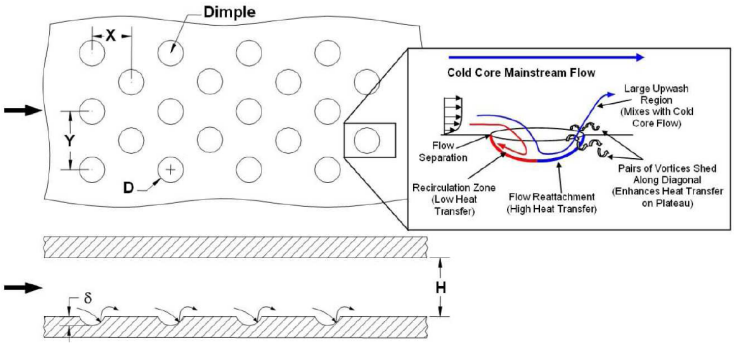

Figure 1.5: A typical test model for dimple cooling studies with a conceptual view of dimple induced secondary flow, [30].

Heat transfer in a dimpled channel is typically 2 - 2.5 times greater than the heat transfer in a smooth channel with a pressure loss penalty of 2 to 4 times that of a smooth channel, while ribbed surface can have higher heat transfer augmentation but only with higher friction factor augmentation [28]. Dimpled surface performances show little dependence on Reynolds number and channel aspect ratio, but dimple size, dimple depth, distribution, and shape can strongly affect heat transfer distribution in the channel [30].

1.4 Impingement cooling

Impingement systems are widely used in many gas turbine cooling applications. Usually these systems consist of a target plate, for example leading edge in blades or mid-chord region in vanes, that is cooled by multiple impingement rows of orthogonal jets. The cooling air is forced to *impinge* on the blade or vane internal surfaces, and the increased level of turbulence that is generated increases the heat transfer considerably. Single jet impingement cooling is the application of a high velocity coolant mass flow ejected from a hole (or slot) and directed to the target surface.

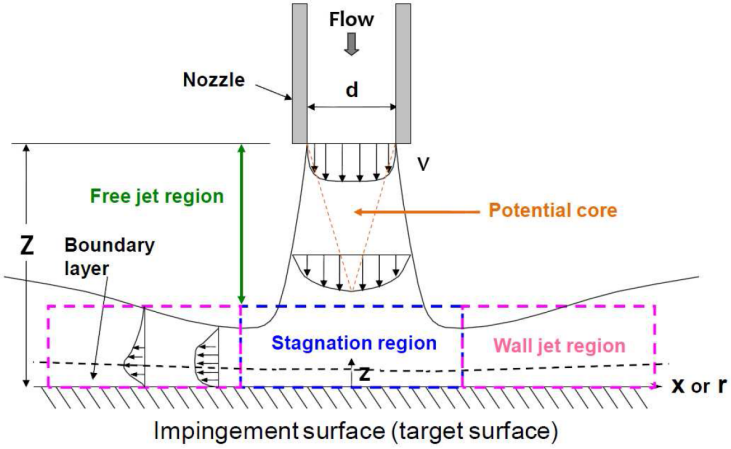

Figure 1.6: Scheme of flow regions in an impingement jet, [31].

Figure 1.6 shows a typical surface impingement caused by a single jet. Flow field of an impinging jet from single round nozzles can be divided into three characteristic regions:

- free jet region
- stagnation region
- wall jet region

In the free jet region, the jet first begins to spread due to intensive shear interaction with the surroundings, which produces entrainment of mass, momentum, and energy. Simultaneously, as the shear layers around the jet grow, the potential core - the region where the velocity is still equal to the bulk velocity - starts decreasing in width. Core is typically visible up to 6 - 7 jet diameters from the nozzle. Once the free jet is fully developed, its axial velocity can be approximated by a Gaussian distribution [19].

A lot of research publications are available about impingement cooling: many works are based on studies performed on a single impinging jet, like the one of Martin [32], Gardon and Akfirat [33] or Bradbury [34], that studied the details of fluid mechanics in a free jet. Sparrow and Wong [35] investigated the effect of jet-to-target plate spacing for a single jet and Goldstein et al. [36] provided variations in single jet heat transfer with considerations of Reynolds number and again by changing jet-to-target plate spacing; Goldstein and Seol [37] compared the heat transfer between a row of circular jet and a slot jet, while an analysis of the crossflow impact on the jet structure was performed in [38] by Goldstein and Behbahani. In gas turbine applications, mostly multiple jets are used instead of an isolated single jet, in the form of two-dimensional arrays of impingement jets: the most frequent configurations is *inline* or *staggered* arrays, as shown in Figure 1.7.

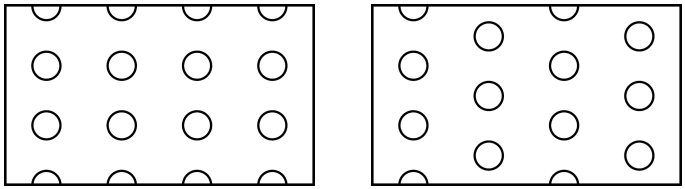

(a) Inline array. *(b) Staggered array.*

Figure 1.7: Typical impingement holes arrays used in gas turbine cooling.

The accumulation of the impinged exhaust fluid in large arrays of impingement jets creates a significant crossflow that interacts in a detrimental way, as shown by Florschuetz et al. [39]. The accumulating

crossflow decreases the peak heat transfer coefficient of the impinging jets, as confirmed by the experimental studies of Kercher and Tabakoff [40] and later by Bailey and Bunker [41]. Depending on the geometric configurations and flow rate, crossflow effect can decrease the row averaged heat transfer coefficient by more than 20% [42]. The work of Kercher and Tabakoff [40] and Florschuetz et al. [39] provide correlations for evaluating the averaged values of Nusselt number on a row-by-row basis and especially the latter is widely used as a valuable design tool [42] also for combustors applications, as confirmed by the experimental campaign performed by Facchini et al. [43]. Correlation developed by Florschuetz et al. [39] can be characterized by non-dimensional parameters, like X/D, Y/D, and Z/D, where X/D and Y/D represent the jet-to-jet spacing in streamwise and spanwise direction respectively, and Z/D gives the jet-to-target plate spacing, all normalized with the diameter D. The effects of these parameters on the Nusselt number evaluation have been studied by Florschuetz et al. [39] and Matsumoto et al. [44]. As expected, increasing jet-to-jet spacing in streamwise or spanwise direction will lead to a decrease in heat transfer coefficient and a larger or jet-to-wall spacing, also produces lower heat transfer. In addition to the geometric factors, the presence of crossflow is another important parameter that affects jet impingement heat transfer performance, as said before: for that reason the ratio of the crossflow mass flux G_c over the jet mass flux G_j directly appears into Florschuetz et al. correlation reported in 1.11 ([39]). A, B, m and n are coefficient that depends on other coefficients C, n_x, n_y, n_z with the form described in 1.12, whose values are reported in Figure 1.8 separately for inline and staggered geometry. Florschuetz correlation is probably the most used in gas turbine component design due to its large range application and geometrical dependence.

$$Nu = A\, Re^m \left\{ 1 - B \left[\left(\frac{Z}{D} \right) \left(\frac{G_c}{G_j} \right) \right]^n \right\} Pr^{1/3} \tag{1.11}$$

$$A\,, B\,, m\,, n = C \left(\frac{X}{D} \right)^{n_x} \left(\frac{Y}{D} \right)^{n_y} \left(\frac{Z}{D} \right)^{n_z} \tag{1.12}$$

	Inline Pattern				Staggered Pattern			
	C	n_x	n_y	n_z	C	n_x	n_y	n_z
A	1.18	-0.944	-0.642	0.169	1.87	-0.771	-0.999	-0.257
m	0.612	0.059	0.032	-0.022	0.571	0.028	0.092	0.039
B	0.437	-0.095	-0.219	0.275	1.03	-0.243	-0.307	0.059
n	0.092	-0.005	0.599	1.04	0.442	0.098	-0.003	0.304

Figure 1.8: Coefficients for Florschuetz correlation, [39].

1.5 Film cooling

There is no better way to describe film cooling than using Goldstein's definition: "Film Cooling is the introduction of a secondary fluid (coolant or injected fluid) at one or more discrete locations along a surface exposed to a high temperature environment to protect that surface not only in the immediate region of injection but also in the downstream region"[36]. This definition underlines that film cooling is not a *cooling* method but a protection system aimed at generate a thin layer of coolant around hot surfaces: since coolant is at a lower temperature than the mainstream, heat transfer into the airfoil is reduced. Film cooling is widely used on blades, nozzles and endwalls; in Figure 1.9 cooling flows in a nozzle guide vane can be appreciated.

One of the most important parameter used to characterize film cooling performance and having a predominant effect on airfoil design process is adiabatic effectiveness η_{aw}:

$$\eta_{aw} = \frac{T_g - T_{aw}}{T_g - T_c} \tag{1.13}$$

where T_g is gas temperature, T_c is coolant temperature and T_{aw} is the adiabatic wall temperature. When η_{aw} is equal to zero, it means that film

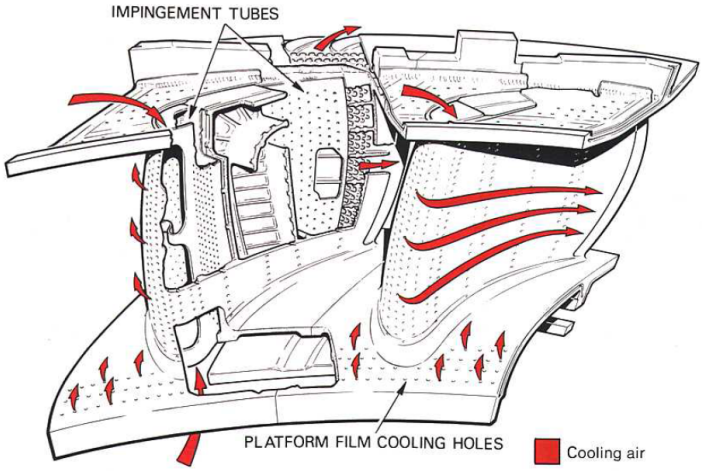

Figure 1.9: Schematic cooling flows in a Nozzle Guide Vane, [18].

cooling is not present and T_{aw} coincides with the hot gas temperature T_g. When η_{aw} is equal to 1.0, it means that the film generates a complete protection of the blade and T_{aw} coincides with coolant temperature T_c. Another parameter used for defining film cooling performance is $NHFR$ (Net Heat Flux Reduction), defining the ratio of reduction in the heat transfer to the blade with film cooling to the one without film cooling:

$$NHFR = 1 - \frac{\dot{q}}{\dot{q}_0} = 1 - \frac{HTC}{HTC_0}(1 - \eta_{aw}\Theta) \tag{1.14}$$

$$\Theta = \frac{T_g - T_w}{T_g - T_c} \tag{1.15}$$

where Θ is the non-dimensional temperature. Adiabatic effectiveness has to be high enough to compensate HTC enhancement due to film cooling, otherwise the overall heat load can not be reduced [45].

Ideally, a film of coolant had to be introduced using a slot with an angle almost tangential to the surface in order to provide a uniform coolant layer. However, long slots would seriously reduce the structural strength of the airfoil, and hence are not feasible. For that reason coolant is usually introduced using rows of cylindrical holes; a major advancement has been achieved in the past years due to the introduction of an exit shaping on the holes allowing a lower momentum coolant injection with a greater surface area [46].

Most important correlations for evaluating film cooling adiabatic effectiveness are dependent from geometrical and fluid dynamic conditions; non dimensional parameters like blowing ratio BR (Eq. 1.16), velocity ratio VR (Eq. 1.17), density ratio DR (Eq. 1.18) and momentum flux ratio I (Eq. 1.19) are defined in order to characterize film cooling behavior and the phenomena related to jet-crossflow interaction. Generally, the most influencing parameter is the blowing ratio, representing the jet momentum augmentation compared to the main flow momentum, for constant DR values.

$$BR = \frac{(\rho v)_c}{(\rho v)_g} \tag{1.16}$$

$$VR = \frac{v_c}{v_g} \tag{1.17}$$

$$DR = \frac{\rho_c}{\rho_g} \tag{1.18}$$

$$I = \frac{(\rho v^2)_c}{(\rho v^2)_g} \tag{1.19}$$

Film cooling holes shape can be different from cylindrical: many studies have been performed over the years for increasing coverage and adiabatic effectiveness values. Most used configurations are slot cooling, Figure 1.10a, and shaped hole cooling, Figure 1.10b; a detailed state of the art including innovative geometries and techniques is reported by Bunker [47].

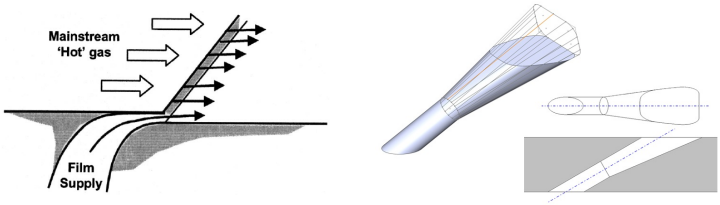

(a) Slot cooling geometry, [47].

(b) Public shaped hole geometry, developed by Penn State University [48].

Figure 1.10: Most used film cooling configurations in gas turbine components.

Most used adiabatic effectiveness correlation used in gas turbine cooling are developed by L'Ecuyer and Soechting [49] and Baldauf et al. [50] for cylindrical holes, while for slot cooling in gas turbines, the most famous is the one developed by Goldstein et al. [51]. Regarding shaped holes, Colban et al. developed a very useful correlation [52] considering outlet over inlet area ratio and the exit area modification when using trapezoidal shape instead of a cylindrical one. Technical literature does not offer open theoretical expressions or correlations to predict film effectiveness in the case of multi-rows configurations. Therefore, it is necessary to adopt theoretical approaches to take into account film cooling superposition effects. Among the few published works concerning film superposition, the most relevant is the model proposed by Seller [53] which is observed to be sufficiently accurate to predict the adiabatic effectiveness distribution at least for the first rows of holes (see for example the works by Harrington et al. [54], Ceccherini et al. [55]). An energy-based model for predicting the additive effect of multiple film cooling rows is recently proposed by Kirollos and Povey [56], comparing its predictions with CFD data and with the Sellers method: the proposed model is shown to be advantageous in situations where energy conservation is required to avoid under-prediction of adiabatic effectiveness.

1.6 Advanced cooling schemes

In a typical nozzle or blade used in gas turbine, previously cited cooling and protection systems are used together, increasing the geometry complexity: an example of a complete *NGV* cooling system can be seen in Figure 1.9, where impingement, turbulated channels and film cooling are shown in the airfoil's section. Both industrial and academic *R&D* activities are focused on analyzing the effects of combining different cooling systems together, always in order to maximize thermal performances, like *Lamilloy* [57, 58], that consists of a mix of impingement holes, pin-fins and film cooling, Figure 1.11.

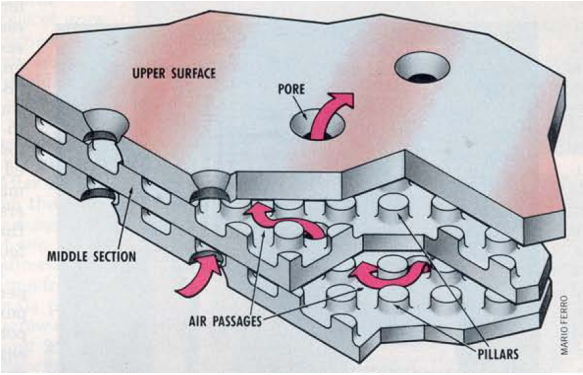

Figure 1.11: Allison's Lamilloy cooling method, [57].

This cooling systems is developed by Allison Advanced Development Company and it's composed by different metal sheets joined together in order to create a sort of transpiration cooling or micro-cooling [12]; impingement and film cooling holes are staggered and interrupted by pin-fins, with the goal of maximize the heat transfer surface and increase thermal performance. Other combined systems can be for example impingement with turbulators [59, 60, 61], impingement and dimples [62, 63] or pin-fins and dimples [64, 65]: geometrical schemes of these cooling systems are shown in Figure 1.12.

Double wall solution is a cooling system developed with the goal of widely increase the heat transfer total area by creating a small gap between internal and external blade surfaces in which the cooling air can flow. Flow inside the double wall can move radially with a multi-pass geometry, axially going counterflow respect to hot gas or just in a small portion of the blade with the only goal to feed specific film cooling holes. It's not easy to find open literature works dealing with double wall geometries, since they have a strong impact on industrial design practices: for that reason many double wall geometries are patented and some of the most interesting configurations are reported in Figure 1.13.

Innovative film cooling holes and cooling systems described before can be very interesting in terms of adiabatic effectiveness and heat transfer performance respectively, but difficult to be realized using casting, EDM (Electrical Discharge Machining), chip removal or in general subtractive manufacturing techniques. With an increasing complexity in gas turbine component's cooling system geometry, innovative strategies like using additive manufacturing techniques (3-D printing) can be mandatory. Recent developments in this field, like the possibility of using titanium or nickel alloys powder in DMLS, or the development of new thermal treatments for increasing component strength and resilience, allows to directly produce gas turbine nozzle or blade starting from a 3D CAD drawing. Many 3-D printed components are at this moment mounted on operative jet engines, after receiving the approval from United States FAA (Federal Aviation Administration) [66]. Some authors are working to find a way for evaluating the better build direction or surface roughness (and its effect on fluid flow and heat transfer) with the use of CT scan [67, 68] and even if there are still many problems in predicting residual stresses accumulated during the build [66] and we are far from having design guidelines or best-practices, additive manufacturing techniques can totally rewrite the rules of how engineers design and realize the entire gas turbine component with its integrated cooling system.

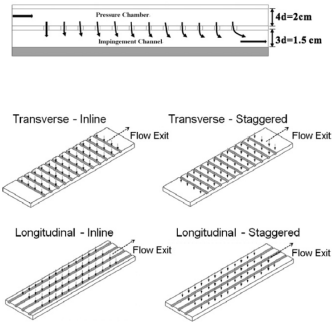

(a) Impingement on different grooved surfaces, [60].

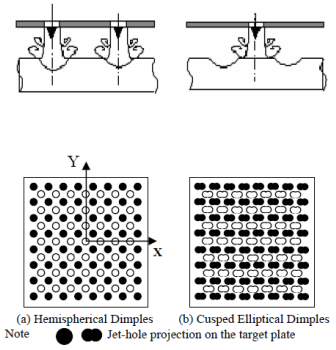

(b) Impingement on dimpled surfaces, [62].

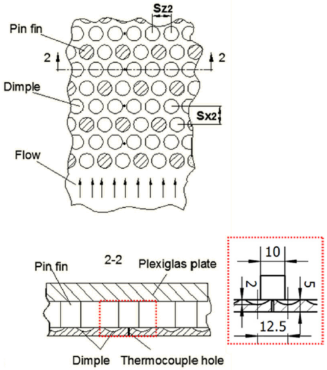

(c) Pin-fins with dimpled surfaces, [65].

Figure 1.12: Schematic representations of different combined cooling configurations.

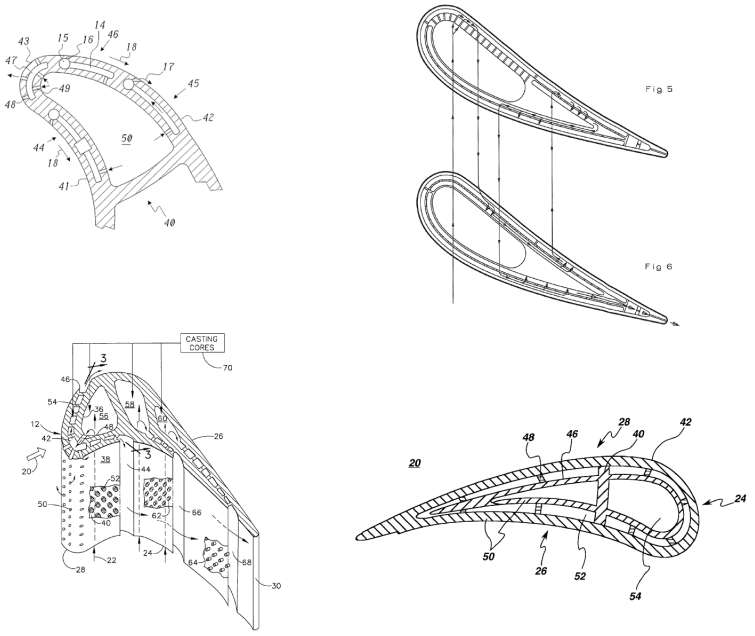

Figure 1.13: Different double wall configurations; from upper left corner, counterclockwise order: local feeding of film cooling holes and counterflow solutions (patent US 6,379,118), axial flow with turbulators and slot cooling (patent US 7,011,502), axial flow (patent US 5,820,337), assoradial impingement with double wall solution (patent US 8,096,766).

Chapter 2

BLANK CODE procedure

This chapter presents a CHT procedure, developed in collaboration with *GE Oil&Gas Nuovo Pignone*® , aimed at predicting metal temperatures on gas turbine blades, nozzles and endwalls, called *BLANK CODE* (BLades And Nozzles networK COnjugate DEsign). Since experimental tests of GT cooling components in operating conditions are very expensive and extremely difficult to realize, numerical procedures are fundamentals in the design phase. For solving the heat transfer problem in a gas turbine and to obtain metal temperature distribution using numerical procedures, two approaches - that differs for the method used for the resolution of the specific equations - are possible: *coupled* and *decoupled*. Coupled approach consists in the simultaneous solution of the equation set which characterizes different domains (fluid for cooling flow and hot gas path and solid for the blade part). In order to rapidly achieve the energy balance on the domains, equations for the two sides should be implicitly coupled: a single problem is hence resolved for both the solid and fluid parts. Main advantage of this method is that the coupling surfaces become part of the solution domain, so continuity of temperature and heat flux at the interfaces is implicitly guaranteed. This approach may lead to a difficult convergence, as reported by Zhenfeng et al. [69]; applications of integrating the two domains into the same solver can be found in [70, 71].

In a decoupled approach, each field is solved separately to establish boundary conditions for the other ones: for this reason information exchange at the interface of contiguous domains becomes necessary. The strategy consists in solving the two fluid domains with a guessed interface temperature, extracting the resulting heat flux and using it as a boundary condition for the Fourier equation in the solid domain: the derived wall temperature is then used to update the fluid calculation. An iterative method is thus necessary to achieve the simultaneous solution of continuity equations of temperature and heat flux.

Several works dealing with conjugate heat transfer problems on gas turbine components can be found in literature; Bohn et al. ([72] and [73]) presented their Conjugate Calculation Technique (CCT) for the analysis of a nozzle guide vane and investigated the film cooling configuration of a leading edge ejection. Takahashi et al. [74] applied a CHT analysis to predict the metal temperature distribution of a three-dimensional first stage rotor blade which had multiple circular passages for internal cooling. Kassab et al. ([75] and [76]) simulated the three-dimensional coupled internal/external flow-field of a realistic film cooled turbine blade; their approach combined Finite Volume Method (FVM) to solve fluid domain and Boundary Element Method (BEM) to solve solid conduction. Other authors turned to alternative methods which use one-dimensional or quasi one-dimensional thermofluid network approaches for the resolution of the internal fluid cooling system. Han et al. [77] developed a model based on flow and energy balance, able of predicting cooling flow characteristics and metal temperature distribution in multipass coolant passages in rotating turbine blades with film cooling. Jelisavcic et al. [78] and Martin et al. [79] used a fluid network approach to perform a multidisciplinary design and optimization of internal cooling passages of cooled turbine blades where a parametric computer model of the three-dimensional internal cooling network was developed while BEM and FEM analysis where applied for heat conduction and internal convection respectively.

Carcasci et al. [80, 81] carried out a blade-to-blade thermal analysis of a PGT10 rotor blade and a vane of PGT2 gas turbine using a correlative

approach to solve the internal heat exchange, while the distribution of the external heat exchange coefficient was determined by *TRAF2D* code [82]. Conductivity in the blade section was studied by a commercial code solving the two-dimensional steady heat equation using the thermal loads got from the convective calculations. Zecchi et al. [83] showed the reliability of a preliminary design stage procedure involving a fluid network approach performing a CHT analysis of 1983 NASA C3X test case [84]. Metal conduction was solved by two-dimensional calculations including only simple cooling ducts without any film cooling holes. A fluid network approach to simulate turbine blade cooling system combined with CFD calculations was used also by Kumar and Prasad [85]; CFD calculations were performed to estimate loss factors and thermal resistances, which were used as input to the fluid and thermal network analysis performed iteratively. More recently, Mohammad Alizadeh et al. [86] developed a decoupled procedure using three-dimensional solvers for the external flow simulation and conduction within metal, while one-dimensional network method is used for the simulation of cooling passages. For validation of the numerical procedure, simulation results were compared with experimental data given by the previously cited 1983 NASA C3X vane. Han et al. [87] devised a program in which both external and internal heat transfer coefficients are obtained through the use of correlations. Blade metal temperatures are obtained from the solution of the coupled equations of mass and energy balance and the model is validated through the NASA EEE blade [88] with an uncertainty of less than $\pm 10\%$ under a set of different boundary conditions.

Andreini et al. [13], starting from the 2D procedure presented by Carcasci et al. [80] and Zecchi et al. [83], developed a quasi 3D iterative procedure to solve a conjugate heat transfer problem in a decoupled way and applied it on a first rotor blade of a heavy duty gas turbine. The procedure consists of an in-house one-dimensional thermofluid network solver to evaluate the thermal loads on coolant side, a 3D CFD analysis to estimate external heat loads and pressure distributions, and a 3D FEM solution to compute heat conduction through the solid. This methodology

has the goal to obtain a sufficiently accurate assessment of the three-dimensional distribution of thermal loads and temperature in a reasonable time, or however reduced, compared to that required by CFD procedures. Heat load on a nozzle or blade airfoil can be strongly influenced by 3D phenomena like hot streak migration [89, 90] an phantom cooling [91], well described by the always improved numerical techniques. For that reason the use of a quasi 3D methodology allow to take into account external heat transfer coefficient and temperature variations due to three-dimensional effects; in Figure 2.1 typical non-uniform heat loads distribution on a HPHT (High Pressure High Temperature) first nozzle is shown. The numerical methodology presented in this chapter is an improvement of the procedure described in [13] and [14].

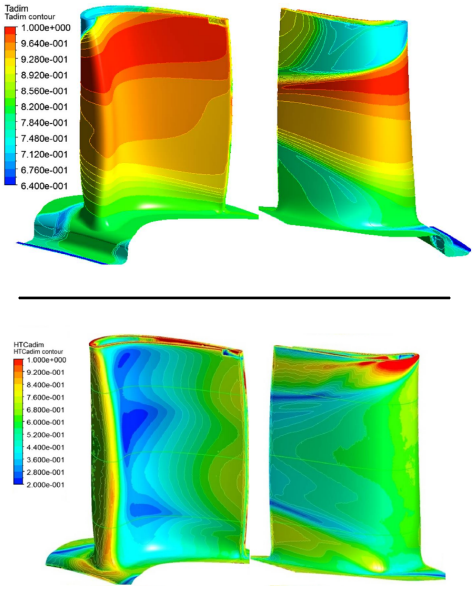

Figure 2.1: Temperature and heat transfer coefficient distribution on a typical first nozzle airfoil [46].

2.1 Procedure description

Wall temperature distribution in a gas turbine component (like a blade, a nozzle or an endwall) can be found by solving 3 separate domains, as represented in Figure 2.2.

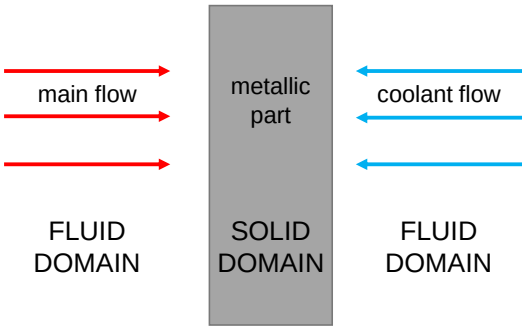

Figure 2.2: Different domains in gas turbine component.

In the presented methodology, external fluid domain - representative of hot gas path - is solved by a 3D CFD simulation, usually carried out by a commercial code like *ANSYS CFX*®, while the conduction through the solid domain is solved by the 3D FEM solver module available into *ANSYS Workbench*®environment. A mono-dimensional fluid network solver, based on a correlative approach for the heat transfer evaluation, is responsible for the solution of the internal fluid domain. The interactions between various solvers, each one solving a specific part of the conjugate heat transfer analysis, are ruled by *ad hoc* developed tools that assure the convergence of the iterative procedure, shown as a simplified block diagram in Figure 2.3.

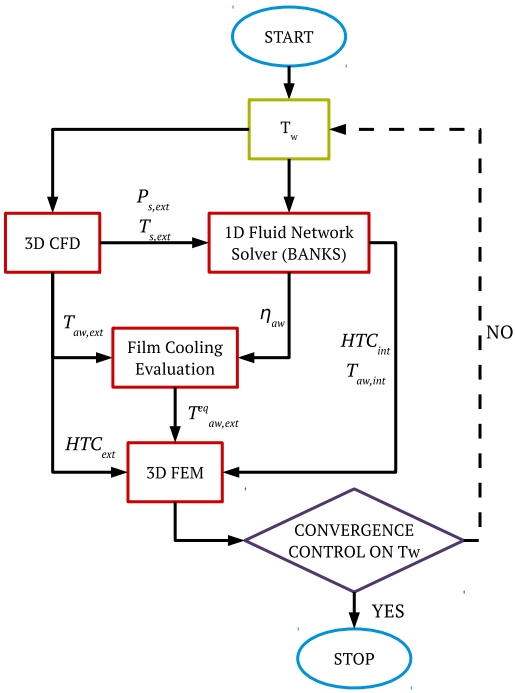

Figure 2.3: Block diagram of the iterative procedure.

3D CFD

Two different 3D CFD computations are performed to determine thermal loads and pressure distribution, necessary to characterize the external flow field. Such CFD simulations do not take into account the presence of film cooling holes on the blade, since the effect of the coolant film will be computed by the 1D fluid network solver, through specific correlations. Only the cooling due to purge flows coming from cavities are completely simulated by CFD. External flow field information, in terms of heat transfer coefficient and adiabatic wall temperature, are necessary as

boundary condition to 3D FEM solver for conduction solution; pressure and temperature distribution are used as input for the 1D fluid network solver to obtain the right pressure ratio and condition for each FC hole.

Two typologies of CFD calculation are necessary: an adiabatic simulation (with the presence of purge flows, if present) to provide $T_{aw,ext}$, $P_{s,ext}$ and $T_{s,ext}$ and a fixed wall temperature simulation to provide HTC_{ext} values. At each iteration of the overall procedure, fixed temperature CFD simulation is carried out by fixing the most updated wall metal temperature distribution coming from the previous FEM results. In order to keep the definition of HTC always consistent, it's important that the adiabatic simulation performed for evaluating heat transfer coefficient is carried out without purge flows.

The expression used for the definition of HTC is therefore:

$$HTC_{ext} = \frac{\dot{q}}{(T_{aw} - T_w)} \tag{2.1}$$

where $\dot{q}$ is the wall heat flux obtained from the fixed wall temperature simulation, T_{aw} is the reference temperature, equal to the adiabatic wall temperature obtained from the adiabatic simulation (without purge flows), and T_w is the wall temperature.

Since the presence of a CFD simulation to be carried out at each iteration can be time consuming, two alternatives approach are presented. The first one allows to perform just two CFD simulations, an adiabatic and a fixed temperature, using a temperature distribution scaled from the adiabatic simulation. This approach allows to save time in the global cycle, assuring a reliable HTC distribution for a design phase. The other approach uses *3 points method* defined by Maffulli et He [92], validated also on a 3D case [93], that allows to find new HTC distribution via analytical way at each iteration by using a correlation linking heat flux to wall temperature; it requires just three CFD simulations (plus the adiabatic one). Further details and verification of the different approaches can be found in Appendix A.

1D Fluid Network Solver (BANKS)

Internal cooling system is modeled using an in-house developed 1D fluid network solver called *BANKS* (Blades And Nozzles networK Solver), which allows a modular approach in solving the coolant domain. Cooling scheme is represented by modules, where each module represents an elementary cooling pattern (for example impingement, film cooling, pin-fin, tube and many others); all the elementary modules can be linked together in a complex fluid network, which is representative of the global blade cooling geometry. *BANKS* solves the fluid network through a one-dimensional steady state analysis: equations solved are the ideal gas law (in its 1D differential form) and mono-dimensional steady state Navier-Stokes equations: mass, momentum and energy continuum. Two different solvers are available: one based on a linear method and one that use a non-linear Newton approach with trust regions, called *TRESNEI* (Trust-REgion Solver for Nonlinear Equalities and Inequalities) [94].

One of the main strengths of *BANKS*, as well as using a one-dimensional approach, is that heat transfer coefficient, friction factor and pressure losses in the models are solved using best-practice correlations. The correlative approach allows an high execution speed of the code, which does not entirely simulate the complex flow physics but it solves some problems, like heat transfer between fluid and blade surface, through empirical analytical expressions. *BANKS* returns internal heat transfer coefficient and adiabatic wall temperature necessary to characterize the boundaries for 3D FEM.

Discharge coefficient C_D is a parameter that summarizes all the losses that limit the mass flow rate through a hole and it is defined as the ratio of the actual mass flow rate to the ideal mass flow rate through the orifice, in which the ideal flow rate is calculated assuming an isentropic one-dimensional expansion from the coolant total inlet pressure (P_0) to the main flow static pressure (P_s), Eq. 2.2.

$$C_D = \frac{\dot{m}}{\dot{m}_{iso}} = \frac{\dot{m}}{P_0 \left(\frac{P_s}{P_0}\right)^{\frac{\gamma+1}{2\gamma}} \sqrt{\frac{2\gamma}{(\gamma-1)RT_0}\left(\left(\frac{P_s}{P_0}\right)^{\frac{\gamma-1}{\gamma}} - 1\right)} A} \tag{2.2}$$

The evaluation of discharge coefficients of impingement or film cooling holes, tubes, and channels, are carried out (when not known by previously conducted experimental or numerical campaign) by using a specific routine called *CDLIB*, based on a correlative approach. Three different correlations are available: the one developed by digitalizing data from Gritsch et al. [95], one based on Reichert et al. correlation [96], and the one developed by Da Soghe and Andreini [97]: each correlation is more indicated in a specific application case, and references can help to better understand their application range.

The modular approach of *BANKS* allows to create very complex fluid network starting from the elementary models, and it allows also to add new modules or correlations by writing specific Fortran subroutines. Complex fluid network, characterized by a large number of mono-dimensional models representing the three-dimensional geometry, can be automatically prepared with a couple of tools, one developed inside NX® environment that allows to export all the geometrical informations of the nozzle, blade or platform, and the other, called *NEST* (NEtwork Setup Tool) that use these exported files for generating all the input files necessary for *BANKS*. Additional information about *NEST* can be found in appendix B.

Film Cooling Evaluation

Film cooling effect is evaluated from the fluid network solver by computing, along prearranged sections of the airfoil or endwall, the adiabatic effectiveness using L'Ecuyer and Soechting [49] or Baldauf et al. [50] correlation for cylindrical holes, Colban et al. [52] correlation for shaped holes an Goldstein correlation for slot cooling [51]. Film superposition effect is handled by the formula proposed by Sellers[53].

Local external conditions required as input by the correlations (gas pressure, velocity and temperature), are obtained from the adiabatic CFD simulation. The resulting distribution of adiabatic film effectiveness is then interpolated on the 3D surface of the airfoil and local values of adiabatic wall temperature predicted by the CFD simulation ($T_{aw,ext}$) are corrected as reported in Equation 2.3, according to the definition of adiabatic effectiveness. Looking at Eq. 2.3, η_{aw} is the local value of adiabatic effectiveness after the interpolation from correlation data and T_c is the coolant temperature exiting from each hole (computed by the fluid network solver).

$$T^{eq}_{aw,ext} = T_{aw,ext} - \eta_{aw}(T_{aw,ext} - T_c) \tag{2.3}$$

A dedicated methodology was developed in order to accurately model heat loads on *lands* (metal part between two slots, Figure 2.4) when slot cooling is present on a nozzle or blade pressure side near trailing edge.

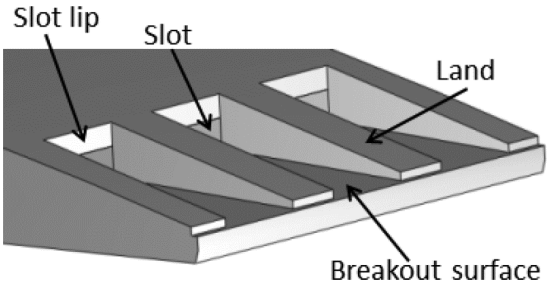

Figure 2.4: Slot cooling scheme on a gas turbine nozzle or blade, [98]

In fact these parts are not affected by the high values of η_{aw} (and by consequence low temperature) typical of slot cooling, but on the contrary film cooling coverage can be very low, because is given only by previous rows that are terminating their effects near TE. High temperature gradients can be generated: so an accurate modeling of slot cooling appear to be mandatory.

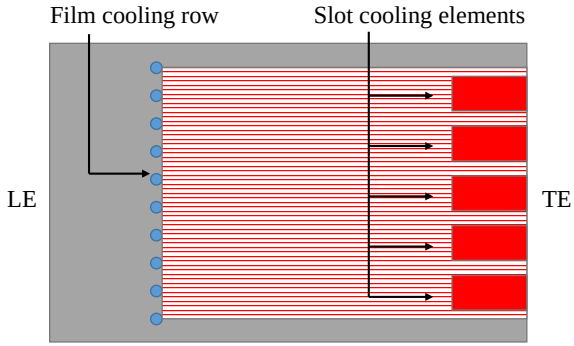

Figure 2.5: Slot cooling modeling in BLANK CODE procedure.

Different heat loads are applied on slot surfaces and land surfaces, as shown in Figure 2.5, where a schematic nozzle's pressure side characterized by one film cooling row and five slot cooling elements is represented. On the surfaces represented by the striped patch, only the presence of the film cooling row is been taken into account, while on the solid colored patch, adiabatic effectiveness of the film cooling row is superposed with the one generated by slot cooling. Using a patch approach for applying mono-dimensional heat loads coming from *BANKS*, will allow to catch three-dimensional phenomena, like the interaction between different temperatures on lands and slot surfaces, in the FEM analysis.

3D FEM

Once external and internal thermal loads are computed, conduction through the metal of the blade can be solved inside a FEM solver. External load values (HTC_{ext} and $T^{eq}_{aw,ext}$), obtained by CFD and film cooling correction, are interpolated on external blade surfaces of FEM mesh (airfoil, endwalls). In the same way internal loads coming from the fluid network solver (HTC_{int} and $T_{aw,int}$) are interpolated on the internal cavities of the blade. All interpolation steps is completely managed by automated

tools coupled with the *ANSYS Workbench*® environment. FEM grid is clustered enough to limit discretization errors due to interpolation process on non-conformal grids.

Since FEM mesh is performed without film cooling holes, heat removal due to forced convection through the holes has been taken into account by using internal heat transfer correlations. A specific tool applies heat transfer coefficient and adiabatic wall temperature evaluated by the fluid network solver to mesh nodes located inside film cooling holes' position. Specific uniaxial elements, called *LINK34*, with the ability to convect heat between their nodes [99], are used to apply a convection condition to those nodes contained inside the 3D space occupied by the hole. This approach allows to avoid film cooling holes meshing, strongly reducing the computational costs, but at the same time realize a heat removal inside the holes, as shown in Figure 2.6 where is clear the effect on final blade temperature but it's also clear that physical holes are not present neither in the geometry, nor in the mesh.

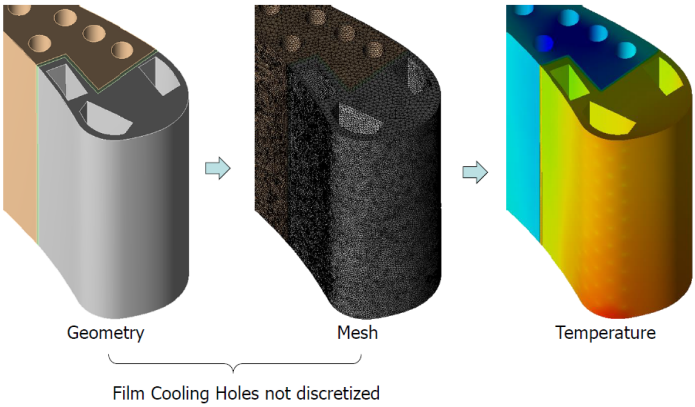

Figure 2.6: Heat removal performed by means of LINK34 elements.

Convergence criteria

The convergence of the global procedure is verified by checking computed wall metal temperature on each mesh node. The procedure convergence is assessed when relative errors between the last two iterations is below a specified value. Usually less than 10 iterations are required to get a convergence with an adequate relative error.

2.2 Validation

Goal of the present section is to validate the above described *BLANK CODE* procedure under different cooling scheme configurations against experimental data. Two typical blade cooling schemes have been considered: one employs ten internal radial cooling channels and the other one adds showerhead and film cooling rows to the previous configuration. Comparisons are presented in terms of airfoil static pressure and metal temperatures; wall temperature comparisons are the best way to understand the capabilities of conjugate procedures, since includes both conduction and convection effects.

2.2.1 Internally cooled vane: NASA C3X 1983

The first analyzed cooling configuration is the one related to 1983 NASA test case, originally presented by Hylton et al. [84]. The test case is representative of a highly loaded, low solidity, internally cooled airfoil, simulated at engine conditions. Many works ([70, 71, 83, 86, 100, 101]) referred to the Hylton et al. report [84] for their codes verification purposes, since it provides a database covering a wide range of operating conditions and geometries, and thus, it represents a significant test for the predictive capabilities of various analytical models. The experiment in fact, provides data concerning a somewhat complete and realistic example of cooling system, allowing to investigate at the same time conduction within metal and internal/external flow with near-engine operating conditions.
Case chosen for simulation is the one called *run 112, case 4422* [84].

2.2.1.1 Geometry description

The geometry, designed by Allison Ltd. and depicted in Figures 2.7 and 2.8, is representative of a linear cascade of a gas turbine first stage. It is characterized by three constant cross-section cylindrical vanes, cooled by air flowing radially through ten smooth-walled channels, almost located along the camber line and discharging at atmospheric pressure. Central vane was instrumented for heat transfer and aerodynamic measurements with each hole fed by a metered line, while the holes of adjacent blades were supplied by a common plenum.

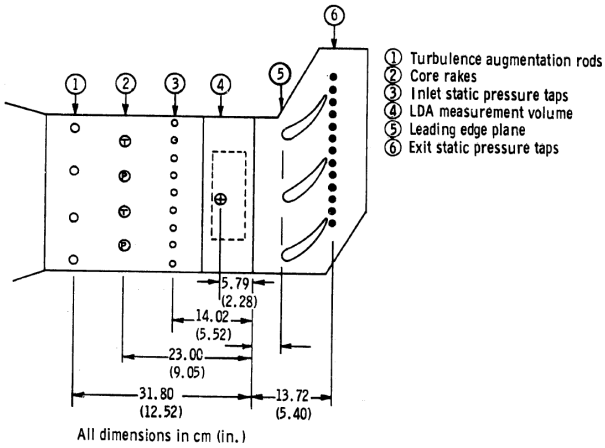

Figure 2.7: NASA C3X 1983 test case: rig geometry (modified from [84]).

Figure 2.8 shows the placement and numbering of the cooling holes. This scheme represents an instance of a closed-loop cooling system, because there is not discharge of coolant coming from the ten radial channels on the blade outside. A natural gas burner upstream of the test section allowed engine-realistic temperatures, turbulence intensities, Mach and Reynolds numbers. Cooling setup was designed to control the mass flow rate of each channels: in fact each one is supplied from a separated metered line.

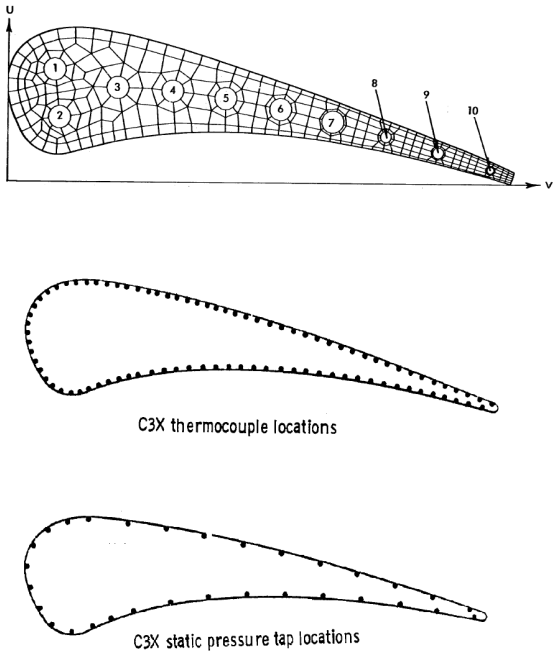

Figure 2.8: NASA C3X 1983 test case: channels position and instrumentation location (modified from [84]).

Detailed information about data reduction and measurement uncertainties can be found in [84].

2.2.1.2 Procedure-supporting CFD simulations

Steady-state CFD RANS calculations have been performed with the commercial 3D Navier-Stokes solver *ANSYS CFX®*. Solid surfaces are treated as smooth, no-slip walls, upper and lower walls are considered adiabatic and only central vane is simulated, delimiting external fluid

domain by periodic boundaries. Flow path boundary conditions have been recovered from Hylton et al. [84], in terms of total pressure, total temperature, turbulence intensity and length scale values at the inlet; outlet pressure conditions is chosen for matching Mach and Reynolds number, since is not directly reported in [84]. Numerical domain is shown in Figure 2.9, while boundary conditions are reported in Table 2.1.

$P0_{g,in}$ [Pa]	$T0_{g,in}$ [K]	Ma_{in} [-]	Re_{in} [-]
321800	783	0.17	$0.53 \cdot 10^6$

Ma_{out}[-]	Re_{out} [-]	Tu[%]	L_d [m]
0.9	$2.01 \cdot 10^6$	8.3	0.005

Table 2.1: Boundary conditions for CFD, as reported in [84].

Compressibility effects have been taken into account and High Resolution advection scheme has been used. Fluid has been modeled as ideal gas with molecular weight of 28.96 $kg/kmol$ and the properties of specific heat capacity cp, thermal conductivity k and viscosity μ, were expressed as function of temperature by correlations fitting the data reported by Rohsenow et al. [102]. Energy equation has been solved in terms of total energy and viscous heating effects have been accounted for. The $k-\omega$ SST turbulence model developed by Menter et al. [103], in its formulation made available by the CFD solver, has been used in conjunction with an automatic near-wall treatment approach. Transition from laminar to turbulent boundary layer has been taken into account employing the $\gamma - Re_\theta$ model available in *ANSYS CFX*®. The choice of turbulence and transition models has been made on the base of a sensitivity analysis against experimental data, reported in [101]. Numerical grid is a $6.96 \cdot 10^5$ elements hexahedral grid (with a y^+ on the blade maintained below 0.5).

In order to validate the external flow field, a comparison of pressure values coming from CFD simulations with the experimental data is presented. The predicted and measured pressure (normalized on $P0_{g,in}$) distribu-

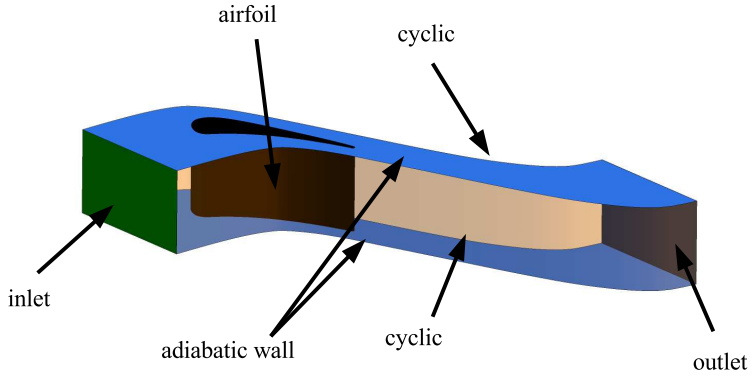

Figure 2.9: NASA C3X 1983 numerical domain for CFD simulations.

tions along X/Ax_{Ch} (local axial coordinate over axial chord length, all the results from now on are presented in this way), on both the pressure and suction sides at the vane midspan, are shown in Figure 2.10. As shown, on the suction side (lower part of the curve in Figure 2.10), the gas flow accelerates rapidly with a corresponding steep descent of pressure from the stagnation line towards the throat, reaching a minimum value of approximately half of the inlet total pressure ($Ps/P0_{g,in} = Ps/P_{ref} = 0.51$) by 40 % of the axial length. Then, due to the subsequent deceleration of the flow, an adverse pressure gradient follows this minimum, and after 70 % a moderate acceleration occurs to the trailing edge. On the entire pressure side, the flow is under a favorable pressure gradient. It starts with a slow acceleration from the leading edge to about 50 % of the axial length, during which pressure stays almost constant near the maximum value, and then speeds up toward the trailing edge, with a consequent pressure fall with further distance towards the trailing edge. CFD results are in good agreement with the measurements, except for a slight divergence between predictions and data on the suction side around $X/Ax_{Ch} = 0.60$.

This small discrepancy also appeared in other works in literature (e.g. [70, 100, 101] and it is probably due to variations of the onset point predicted by the transition model in CFD simulations.

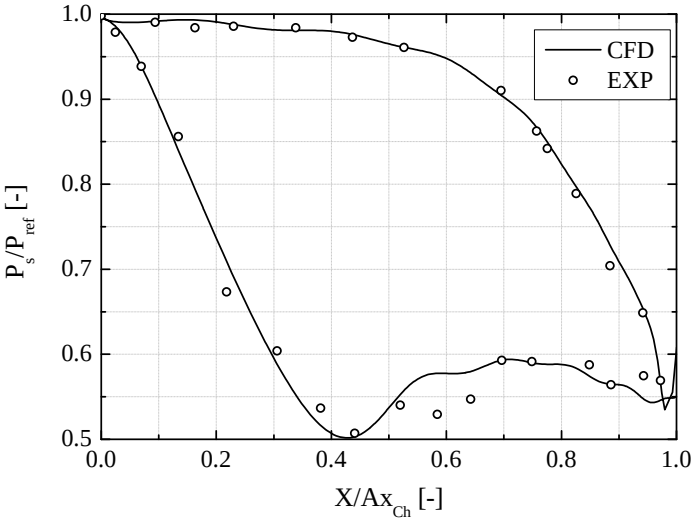

Figure 2.10: NASA C3X 1983 midspan airfoil static pressure compared to experimental data reported in [84].

2.2.1.3 Fluid network setup

Cooling system of test case, as described in section 2.2.1.1, consists of radial channels, fed by a metered line with a calibrated orifice meter for each tube, in order to control inlet pressure and temperature separately for each duct.

The mono-dimensional fluid dynamics is resolved with *BANKS* by modelling each tube with an elementary model representative of a radial tube that carried out the resolution of a stationary flow. Each model is described by specific text input files describing the geometry, compiled using data available in [84].

As regards boundary conditions, a specific value of mass flow rate and average static temperature for each tube were provided in [84]. However Hylton et al. did not provide any information about the inlet total pressure and temperature neither about the inlet static temperature. Since inlet total pressure and temperature values for each tube are required by *BANKS* for the fluid network solution, an iterative process is performed in order to match experimental mass flow rate and average Reynolds number. Static inlet temperature and pressure outlet value are retrieved from [70]. List of boundary conditions given by literature is reported in Table 2.2 while imposed values are specified in Table 2.3.

Channel	1	2	3	4	5	6	7	8	9	10
$\dot{m}$ $[g/s]$	7.79	6.58	6.34	6.66	6.52	6.72	6.33	2.26	1.38	0.68
Re $[\cdot 10^3]$	67.9	57.3	57.0	59.2	60.3	56.1	56.9	39.9	22.1	16.1
T $[K]$	387	388	371	376	355	412	367	356	406	420
$P_{s,out}$ $[kPa]$	100	100	100	100	100	100	100	100	100	100

Table 2.2: NASA C3X 1983 boundary conditions for radial tubes, as reported in [84] and [70].

Channel	1	2	3	4	5	6	7	8	9	10
$P0_{in}$ $[kPa]$	154	139	134	139	135	142	134	201	145	187
$T0_{in}$ $[K]$	412	409	389	396	372	435	384	372	420	433
Ps_{out} $[kPa]$	100	100	100	100	100	100	100	100	100	100

Table 2.3: NASA C3X 1983 boundary conditions for BANKS.

Many heat transfer correlations are available in *BANKS*: in the presented work the ten radial tubes are solved using Gnielinski correlation [21], while differences between Gnielinski and Dittus Boelter correlation are presented in [14].

2.2.1.4 FEM setup

NASA C3X vane had a constant no twist cross-section. Therefore its FEM solid model has been created by extruding the two-dimensional airfoil through the blade height, in the spanwise direction. Airfoil has been created with a spline through points whose coordinates are supplied by Hylton et al. [84]. Solution of the thermal conductive model has been provided by the FEM approach using the three-dimensional Fourier's law solver module of *ANSYS Workbench®*. Numerical grid has been properly refined to characterize each detail without significantly affecting the computational time. Mesh consists of about $6.0 \cdot 10^5$ ten nodes tetrahedral elements (for a total of about $8.9 \cdot 10^5$ nodes), with refinement on the surfaces on which thermal loads have to be applied, like the airfoil and channels' internal surfaces, particularly the last three near the trailing edge, because of the major thermal gradients occurring there. Vane material is specified in [84] and is *310 stainless steel*, which has a constant density of $\rho = 7900\ kg/m^3$ and specific heat of $cp = 585.15\ J/(kg \cdot K)$ over the range of temperatures characterizing the problem. Thermal conductivity was specified to vary with temperature, as assured by Facchini et al. [70], with a linear law, reported in Equation 2.4:

$$k(T) = 6.811 + 0.020176 \cdot T \tag{2.4}$$

2.2.1.5 Results

Numerical results using *BLANK CODE* procedure are now reported in terms of metal temperature distribution. In Figure 2.11 airfoil wall temperature distributions at midspan are reported for the tested case and error bars of $\pm 2\%$ (as reported in [84]) are applied to the experimental data. Figure 2.11 shows a good agreement of the numerical procedure with the experimental data in terms of both values and trends, except on the suction side, where, as shown in Figure 2.10, an under-prediction of external pressure values and hence of the external heat transfer coefficient is present.

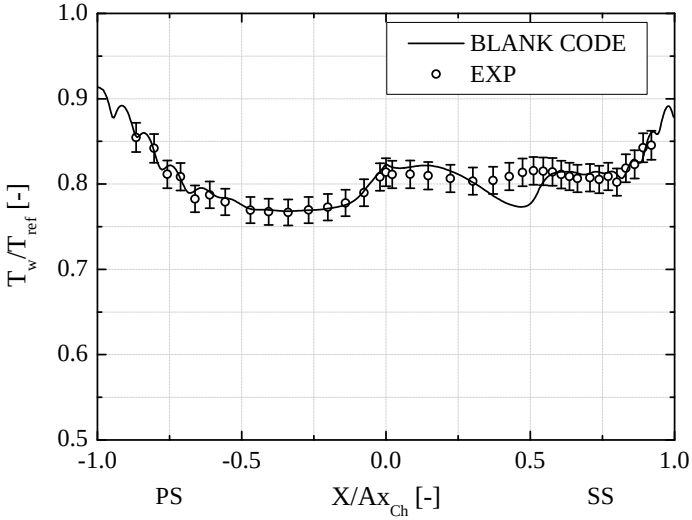

Figure 2.11: NASA C3X 1983 midspan airfoil wall temperature compared to experimental data reported in [84].

2.2.2 Internally and film cooled vane: NASA C3X 1988

The second analyzed cooling configuration is the one related to 1988 NASA C3X test case, originally presented by Hylton et al. [104]. The test case is representative of a highly loaded, low solidity, internally cooled airfoil, simulated at engine conditions and differs from the previously described for the presence of film cooling rows. The vane presents a thermal barrier separating the leading edge and the tail region. Many authors referred to the Hylton et al. report [104], for validating numerical codes (Garg et al. [105], Hall et al. [106], Sarkar et al. [107], Mangani et al. [108]), performing numerical assessment of turbulence model (Ledezma et al. [101]) or sensitivity analyses (Garg et al. [109], Sarkar et al. [110]).

Case chosen for simulation is the one called *44344* [104].

2.2.2.1 Geometry description

Vane profile is the same used in the non film cooled experiments reported in [84]. Central test vane from Figure 2.7 was replaced with a new vane which had film cooling rows on suction side, leading edge, and pressure side. Test vane was initially manufactured as a single piece; after all the film cooling holes, the plena and ten radial channel were machined, the vane was cut into a nose and a tail piece to form a thermal barrier between the film cooled nose part and rest of the vane, Figure 2.12. After the test vane split in two pieces, a shim was welded across the thermal barrier gap on both the pressure and suction surfaces, to provide a smooth continuous surface on the airfoil. Also, the gap was sealed at the two ends of the airfoil, thereby creating a sealed air gap between leading edge region and tail. Air gap provided the thermal barrier, which purpose was minimize cooling effect coming from leading edge plena on tail region: only the ten radial channels and film cooling effect interest trailing edge region cooling. Vane was internally cooled by an array of ten radial cooling channel; each channel of the two slave vanes were supplied from a common plenum, whereas each tube in the test vane was supplied from a separate, metered line. Details of film cooling rows are presented in Figure 2.13.

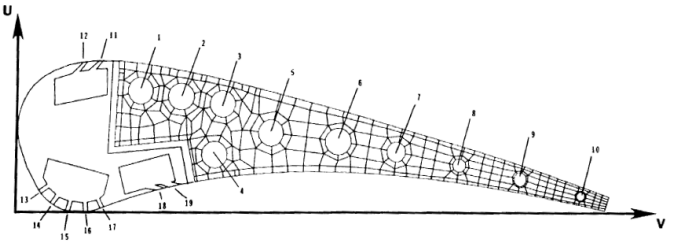

Figure 2.12: NASA C3X 1988: channels and plena position, [104].

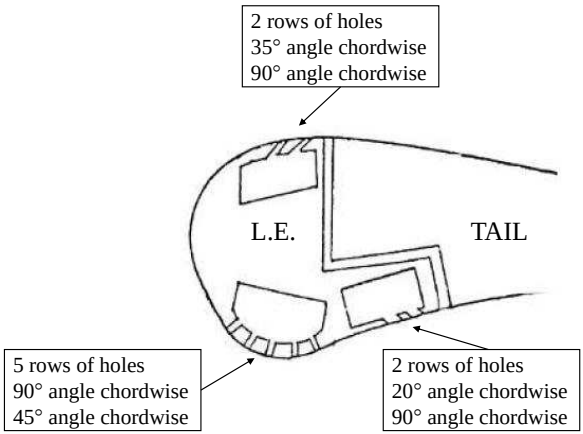

Figure 2.13: NASA C3X 1988: description of film cooling rows.

2.2.2.2 Procedure supporting CFD simulations

Numerical setup for CFD simulations are similar to the one described in section 2.2.1.2: steady-state RANS calculations have been performed with *ANSYS CFX®*. Flow path boundary conditions have been recovered from Hylton et al. [104], in terms of total pressure, total temperature, turbulence intensity and length scale values at the inlet; outlet pressure conditions is chosen for matching Mach and Reynolds number, since is not directly reported in [104]. Numerical domain is shown in Figure 2.9, while boundary conditions are reported in Table 2.4; Tu value (6.5%) is specified in [104].

$P0_{g,in}$ [Pa]	$T0_{g,in}$ [K]	Ma_{in} [-]	Re_{in} [-]	Ma_{out}[-]	Re_{out} [-]
285130	701	0.17	$0.54 \cdot 10^6$	0.89	$2.03 \cdot 10^6$

Table 2.4: Boundary conditions for CFD, as reported in [104].

Fluid setup for CFD simulation is equal to the one described in section 2.2.1.2, except for the presence of fully turbulent condition instead of $\gamma - Re_\theta$ model, since even if CFD simulations are performed without film cooling holes, their presence in the experimental data should modify transition on the blade. Numerical grid has $3.18 \cdot 10^6$ elements.

In order to validate the external flow field, a comparison of pressure values coming from CFD simulations with the experimental data is presented. The predicted and measured pressure (normalized on $P_{ref} = P0_{g,in}$) distributions along $S/Stot$ (non dimensional curvilinear abscissa), on both the pressure and suction sides at the vane midspan, are shown in Figure 2.14. Also in this case CFD results are in good agreement with the measurements, except for some differences between CFD simulation and experimental data on the suction side. This discrepancy also appeared in other works in literature, e.g. Mangani et al. [108], as reported in Figure 2.15, even if results are referred to a different run (# 44155).

2.2.2.3 Fluid network setup

Film cooling and showerhead are modeled by *BANKS* through a module that solve radial flux inside the radial cavity (of generic shape) with coolant ejection through film cooling rows' holes. Geometrical data required to fluid network solver for defining the model, have been retrieved from Hylton et al. [104]. Concerning the radial cooling channels, in the experimental setup, ducts were fed in the same way described in [84]. However, whereas NASA C3X 1983 report [84] provided documentation of the radial coolant channel flow, NASA C3X 1988 report [104] did not. Coolant supply conditions were not documented in [104] and literature too is poor about these informations. Studies carried out by Ledezma et al. [101] had result as one of the most exhaustive concerning information about boundary conditions. In their work the authors present an inverse procedure for finding mass flow rate and total inlet temperature for each channel. From geometry, external wall heat transfer coefficient and metal temperature distributions retrieved in [104], cooling flows has been calculated in order to match the experimental metal temperature

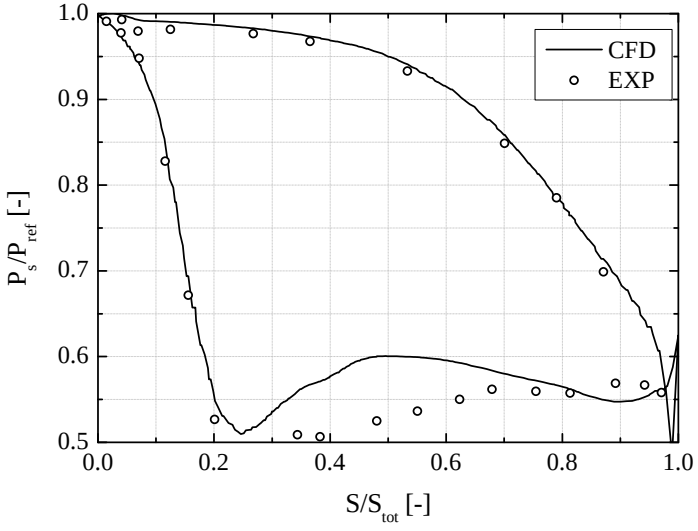

Figure 2.14: NASA C3X 1988 midspan airfoil static pressure compared to experimental data reported in [104].

distribution at midspan. However they provided boundary conditions only for case 44344 and for this reason it has been chosen for the present analysis; radial channels boundary conditions are reported in Table 2.5, while data imposed in *BANKS* matching these values are reported in Table 2.6. Boundary conditions for film cooling plena are retrieved from [104] and reported in Table 2.7; discharge pressures are automatically interpolated from CFD flow field for each film cooling hole.

Channel	1	2	3	4	5	6	7	8	9	10
$\dot{m}$ $[g/s]$	7.84	7.93	7.94	8.26	7.48	6.91	7.52	7.70	4.73	3.57
$T0_{in}$ $[K]$	425	367	351	403	325	327	361	422	380	421

Table 2.5: NASA C3X 1988 boundary conditions for radial tubes, as reported by Ledezma et al. [101].

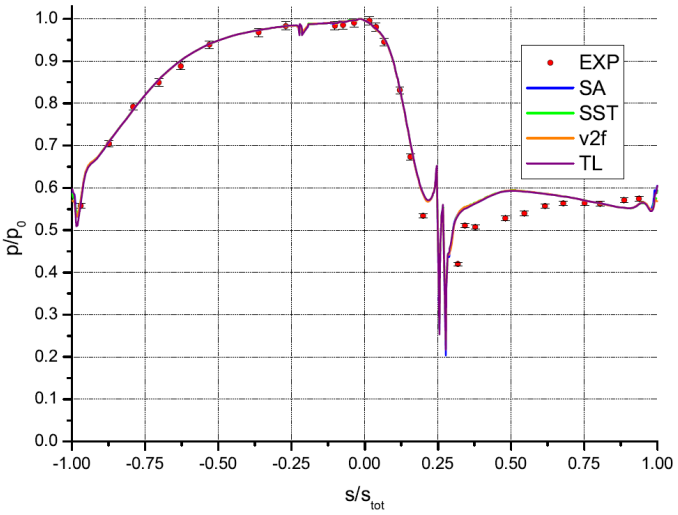

Figure 2.15: NASA C3X 1988 midspan airfoil static pressure compared to experimental data reported in [104] (Mangani et al. [108]).

Channel	1	2	3	4	5	6	7	8	9	10
$P0_{in}$ $[kPa]$	153	148	146	156	139	134	242	636	384	796
$T0_{in}$ $[K]$	425	367	351	403	325	327	361	422	380	421
Ps_{out} $[kPa]$	100	100	100	100	100	100	100	100	100	100

Table 2.6: NASA C3X 1988 boundary conditions for BANKS.

	$P0_{in}/P0_{g,in}$ $[-]$	$T0_{in}/T0_{g,in}$ $[-]$	$\dot{m}$ $[kg/s]$
Suction Side	0.85	0.01340	0.0296
Leading Edge	0.86	0.00638	0.0141
Pressure Side	0.83	0.00752	0.0166

Table 2.7: NASA C3X 1988 boundary conditions for film cooling plena, as reported by Hylton et al. [104].

In the presented work, both radial tubes and film cooling plena are solved using Gnielinski correlation [21], while differences between Gnielinski and Dittus Boelter correlation are presented in [14]. Same correlation is used also for evaluating heat transfer coefficient inside film cooling holes, while adiabatic effectiveness is calculated using L'Ecuyer and Soechting correlation [49].

2.2.2.4 FEM setup

As for the previous case, boundary conditions are both the internal and external thermal loads derived from CFD (corrected with film cooling) and fluid network solver interpolated on blade surfaces. Thermal conductivity values of leading edge and tail bodies is recovered from Eq. 2.4. Concerning the thermal barrier, in the experiment insulation was guaranteed by the presence of air in the gap between nose and tail. Therefore, the metal bodies are separated in FEM simulation; the numerical grid consists of about $9.8 \cdot 10^5$ tetrahedral elements (with ten nodes, for a total of about $1.5 \cdot 10^6$ nodes).

2.2.2.5 Results

Numerical results using *BLANK CODE* procedure are now reported in terms of metal temperature distribution. In Figure 2.16 and 2.17 airfoil wall temperature distributions at midspan, separately from pressure side and suction side, are reported for the tested case and error bars of $\pm 2\%$ (as reported in [104]) are applied to the experimental data.

Both Figure 2.16 and 2.17 shows a very good agreement of the numerical procedure with the experimental data in terms of both values and trends, except some difference on the beginning of instrumented pressure side near the separation zone between the two regions. These differences can be related to the fact that tail and nose regions are physically separated in the simulation, while in the experimental set are insulated but obviously not in a perfect way.

This chapter showed the validation of *BLANK CODE* procedure using two different experimental test cases, with and without film cooling

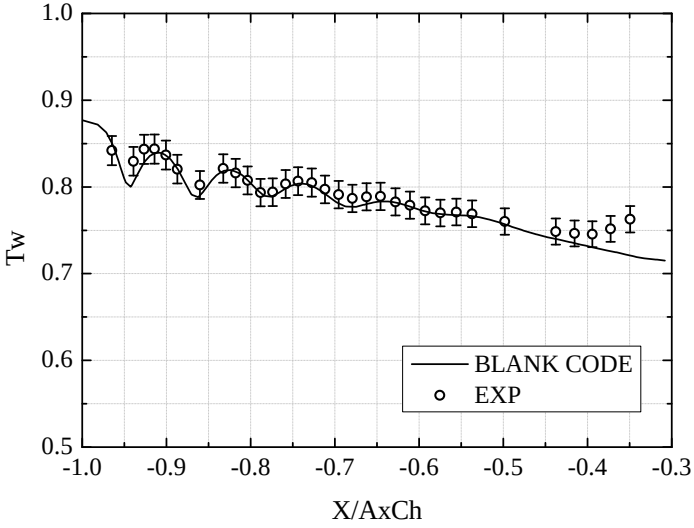

Figure 2.16: NASA C3X 1988 midspan airfoil wall temperature on pressure side compared to experimental data reported in [104].

presence. Results in terms of metal temperature distribution underlined in both cases the predicting abilities of the procedure.

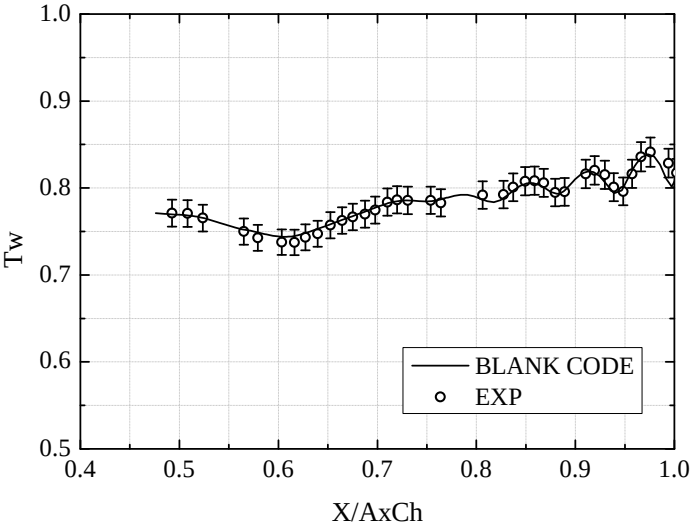

Figure 2.17: NASA C3X 1988 midspan airfoil wall temperature on suction side compared to experimental data reported in [104].

Chapter 3

Innovative impingement

Development of DMLS opens up new horizons regarding the realization of metallic GT components: with additive manufacturing techniques, extremely complex structures (unattainable with traditional methods) are now potentially feasible. For this reason in the next two chapters will be described innovative geometries of two of the most common cooling techniques in vane and endwalls: impingement and film cooling.

Object of this chapter is to analyze and improve an innovative impingement geometry originally developed by Facchini et al. [111] whose goal is to strongly reduce the negative effect of the crossflow on the heat transfer performance, especially in the last rows of large impingement arrays. Innovative configuration will be analyzed by performing fully coupled CFD CHT simulations and by using *BLANK CODE* procedure, which implements Florschuetz correlation [39] (1.11). After that an experimental campaign of an innovative configuration will be carried out and the results will be compared with the one retrieved from *BLANK CODE* procedure.

3.1 Geometry description

The proposed geometry was designed by Facchini et al. [111] and in Figure 3.1 the original design is reported. The proposed geometry

has the goal to strongly decrease negative effects of crossflow increasing from leading edge (LE) to trailing edge (TE) with the presence of a wall that interrupt it. Spent air coming from jet holes located in part A goes into the inlet of part B and its first rows are not obviously affected by crossflow; the feeding air for part A and C remains the same respect to a classic impingement configuration. The positive effect caused by crossflow reduction in part B can be countered by the higher inlet temperature for the impingement holes in this part: it's important to accurately study the innovative system in order to have an effective increase in cooling performances. Another negative effect in this configuration is the increasing pressure drop due to the wall presence that fluid had to overcome in order to feed part B impingement holes.

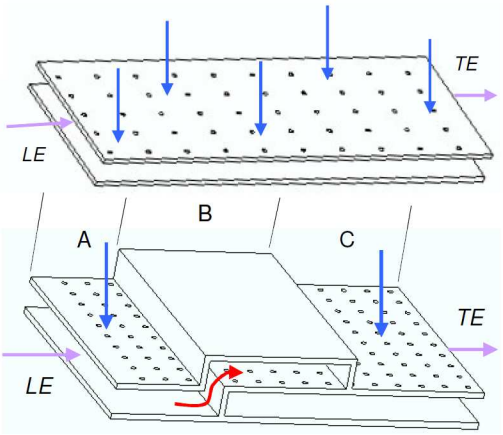

Figure 3.1: Comparison with reference and innovative impingement geometry [111].

For understanding the improvement given by innovative configuration, a comparison with a classic *inline* impingement array was carried out. Typical geometrical values of industrial gas turbine nozzle's impingement system are chosen for characterizing the *Reference* array, as shown in Table 3.1. For a coherent comparison, reference and innovative geometries

have the same global dimensions, the same air flow passage and are fed with the same massflow rate. The proposed geometry - called *Innovative* - is described in Table 3.2.

Zone	Diameter [mm]	Spanwise Holes	Streamwise Holes	X/D	Y/D	Z/D
A	0.4	24	5	10.0	6	2
B	0.4	24	5	10.0	6	2
C	0.4	24	5	10.0	6	2

Table 3.1: Reference geometry parameters.

Zone	Diameter [mm]	Spanwise Holes	Streamwise Holes	X/D	Y/D	Z/D
A	0.4	24	7	6.58	6	2
B	0.4	24	5	9.75	6	2
C	0.4	24	8	6.09	6	2

Table 3.2: Innovative geometry parameters.

3.2 CHT CFD calculations

For comparing the reference and innovative geometries, two fully coupled CFD CHT analyses were performed with commercial code *ANSYS CFX®*. The numerical domain used in the CFD CHT simulations is reported in Figure 3.2 where it's possible to see a fluid domain representing the coolant flow and two solid domains representing impingement plate and gas turbine blade. The numerical domain represented in Figure 3.2 it's representative of reference geometry but the same features can be found in the innovative numerical domain. Two inlets, one for impingement holes and one for the imposed crossflow, and one outlet were present; only a smaller part of the global plate were studied thanks to the presence of symmetry boundary conditions. Hot gas domain has not been simulated but a forced convection condition it's imposed, with typical values of external heat transfer coefficient and adiabatic wall temperature on a gas turbine vane.

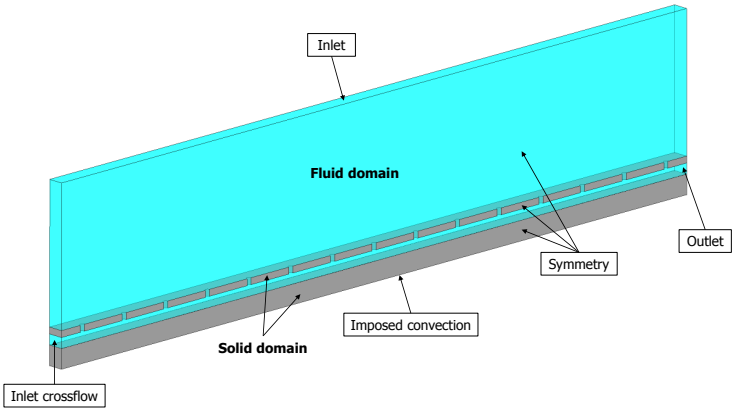

Figure 3.2: Numerical domain for reference case.

Fluid domain has been modeled as ideal gas and the properties of specific heat capacity, thermal conductivity and viscosity were expressed as function of temperature. Energy equation has been solved in terms of total energy and viscous heating effects have been accounted for. Menter's et al. [103] *k-ω SST* turbulence model, in its formulation made available by *ANSYS CFX*®, has been used. All the simulations were performed imposing massflow at the inlet and static pressure at the outlet.

Numerical grid, shown in Figure 3.3, is generated with *ANSYS Meshing*® inside the *Workbench* environment; it is composed by an hybrid (tetra and 20 prism layers at the solid walls) unstructured mesh. A sensitivity was performed in order to assess the impact on the predicted Nusselt number and temperature distribution changing three different meshes, with 13, 20 and 33 millions cell. All the numerical results showed a substantial insensitivity to the grid's dimensions for meshes with more than 20 millions cell, maintaining a value of y_+ less than 1 in all the domain.

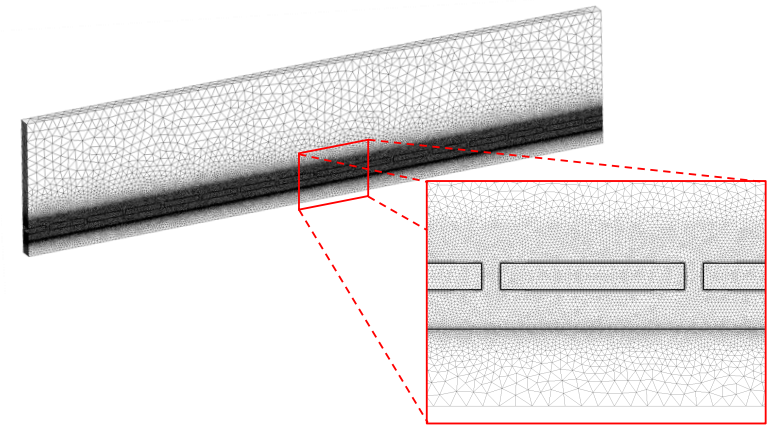

Figure 3.3: Numerical grid used in CFD CHT simulations; reference case is shown.

Numerical results and comparisons

The innovative geometry was compared with the reference one and the results in terms of external temperature and impingement heat transfer coefficient is reported in Figure 3.4 and Figure 3.5, where data are nondimensionalized by a nominal heat transfer coefficient and temperature value and plotted respect to axial abscissa over total length L. As we can see from Figure 3.4, with innovative geometry we can obtain a higher HTC in the last part of the geometry; HTC is always evaluated using the total temperature of the jets as the reference temperature (as performed by Florschuetz et al. [39]). Looking at external wall temperature results in Figure 3.5 we can see that the higher jet temperature values in the central part of the geometry and the different pressure values necessary to obtain the same massflow rate have a detrimental effects on the performances. These results show that an improvement in the geometry design is necessary in order to achieve a more uniform temperature distribution and to obtain lower temperature values.

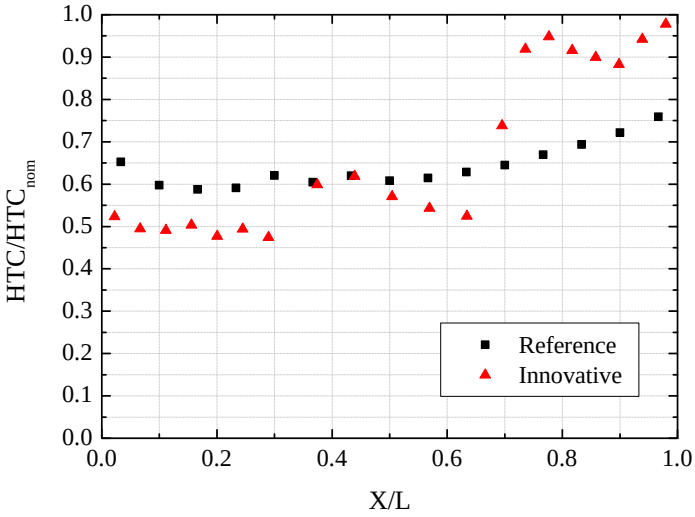

Figure 3.4: Impingement HTC comparison between reference and innovative cases.

3.3 Geometry redesign

The use of a fast procedure to have a correct estimation of the metal temperatures becomes mandatory due to the high computational cost underlined by the previously reported simulation and the necessity of performing multiple runs in order to have a more constant temperature distribution or just to perform a sensitivity analysis. Since a decoupled approach allows to choose the best method for solving each domain, an interesting solution can be the use of *BLANK CODE*. A block diagram of the iterative procedure, slightly modified from the one described in Chapter 2.1 and shown in Figure 2.3 (3D CFD part is not present), is reported in Figure 3.6.

A comparison between CHT CFD and *BLANK CODE* is here presented, both for reference and innovative cases. All the simulations performed with *BLANK CODE* are carried out using *CDLIB* (See Chap-

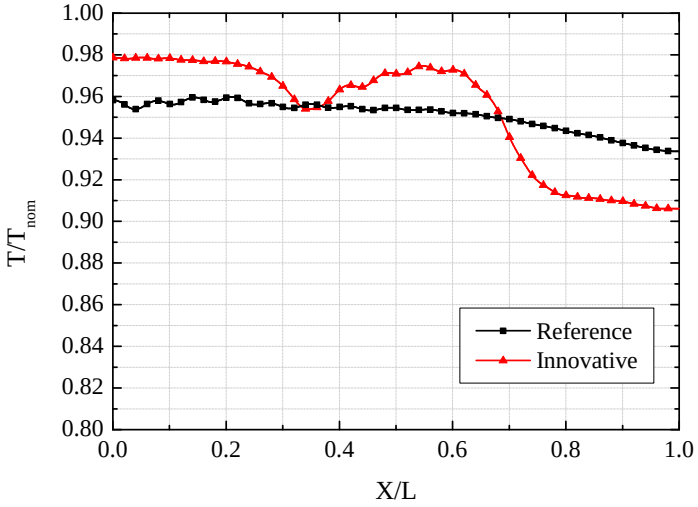

Figure 3.5: Wall temperature comparison between reference and innovative cases.

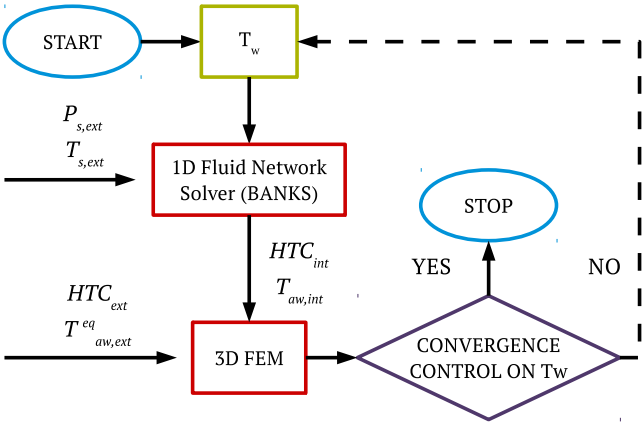

Figure 3.6: Block diagram of the iterative decoupled procedure.

ter 2.1) with Gritsch et al. correlation [95]. Results in terms of external wall temperatures, nondimensionalized by a nominal temperature value, are reported in Figure 3.7 and in Figure 3.8. Some differences can be appreciated in terms of effective temperature values: these differences are related to the mono-dimensional simplification of the problem, and is obviously emphasized in the innovative geometry, where pressure losses between part *A* and part *B* are not well predicted, and part *B* jet holes feeding can be quite far from an homogeneous case, like the one modeled with *BANKS*. Although these temperature differences, limited to a maximum of just 3 percentage points in the worst case, the decoupled procedure seems to well catch the global behavior of the impingement model, and so it can be used to perform multiple runs in order to find the best design for this particular configuration.

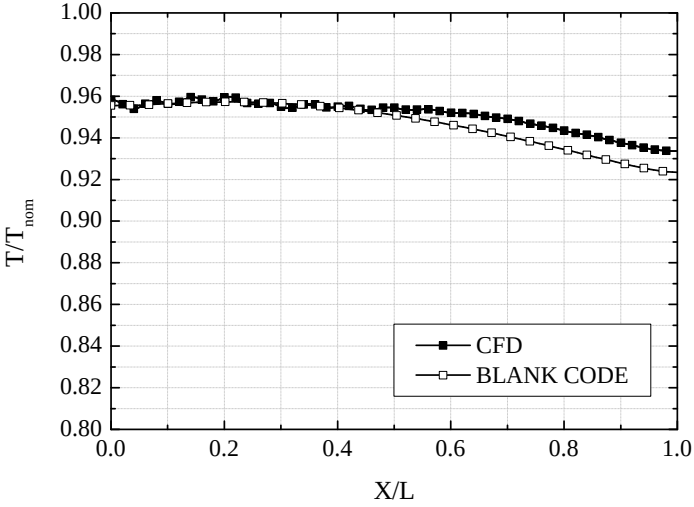

Figure 3.7: Reference case, wall temperature comparisons between CFD and BLANK CODE

Since *BLANK CODE* shows good predictable capabilities in a significantly lower computational time, multiple runs were carried out to

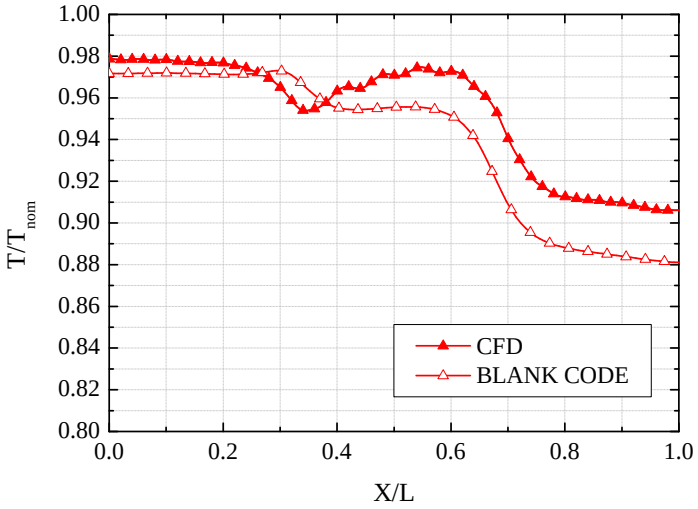

Figure 3.8: Innovative case, wall temperature comparisons between CFD and BLANK CODE

find the most influential parameter that can achieve a better temperature distribution and a lower average value. These simulations indicated that reducing the length of part A and increasing the length of part C may results in an increase of the uniformity of temperature distribution. Also doubling the number of streamwise holes in part B and increasing the number of streamwise holes in part A while reducing it in C can help to reach the best performance of the innovative geometry. The proposed solution is reported in Table 3.3, and it was then validated again with a CHT CFD simulation, with the same setup described in Chapter 3.2: the results in terms of temperature distribution, shown in Figure 3.9, are completely coherent with the innovative geometry, reported in Figure 3.8, even if there are more differences due to a larger number of jet rows in part A and B respect to innovative case.

Finally, a comparison between reference, innovative and improved innovative case in terms of external wall temperature nondimensionalized

by a nominal value is reported in Figure 3.10, where we can see a lower averaged values and a more uniform temperature distribution.

Zone	Diameter [mm]	Spanwise Holes	Streamwise Holes	X/D	Y/D	Z/D
A	0.4	24	9	6.25	6	2
B	0.4	24	10	5.00	6	2
C	0.4	24	6	7.29	6	2

Table 3.3: Improved innovative geometric parameters.

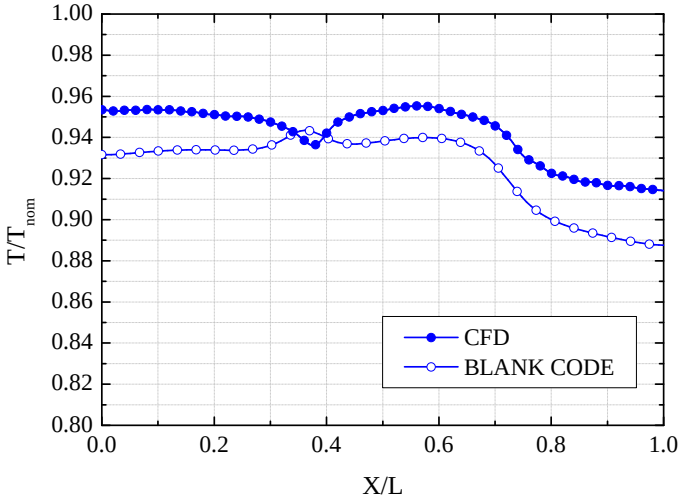

Figure 3.9: Improved innovative case, wall temperature comparisons between CFD and BLANK CODE

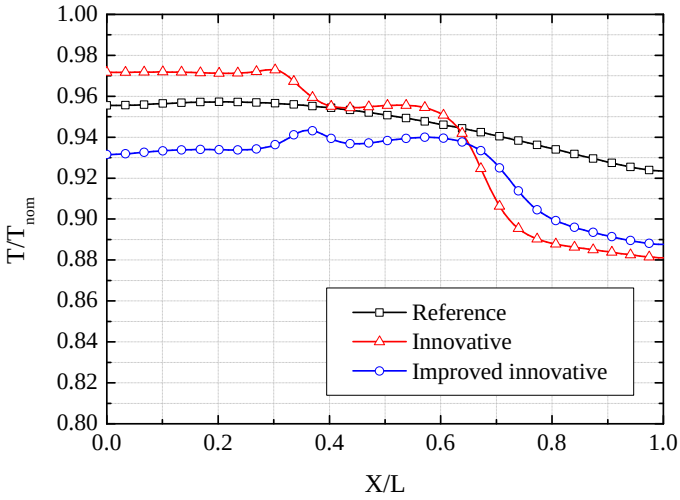

Figure 3.10: Comparison of reference, innovative and improved innovative geometries.

3.4 Application on a second stage HPT

The sensitivity analysis performed with the decoupled procedure allows to understand the most influential parameters in the innovative geometry impingement design: these information were used with the goal of replacing a standard impingement baffle located in a second stage gas turbine vane with the innovative one. The simulation, performed with *BLANK CODE*, was carried out maintaining the same massflow rate and the same external condition. A scheme of the innovative geometry compared with the one actually mounted on the vane (called *standard*) is shown in Figure 3.11.

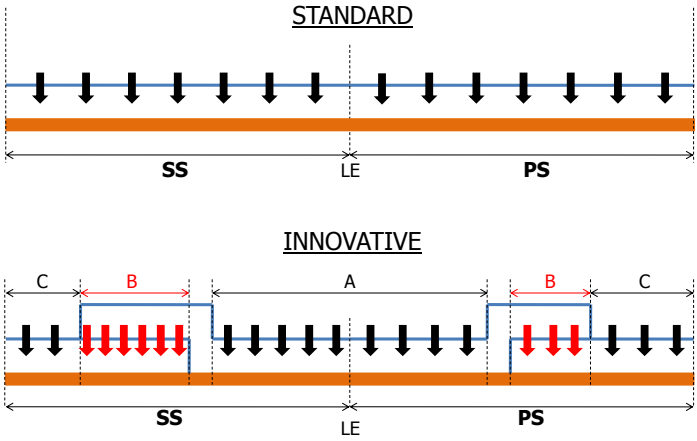

Figure 3.11: Different impingement geometries.

There are a large number of holes in the standard configuration, so a large amount of crossflow is present near to the trailing edge: for that reason the innovative geometry can increase the cooling performance by avoiding a weakened heat transfer coefficient near the end of the vane, due to spent air disturbing and decreasing the impingement effect. The results in terms of non-dimensional external wall temperature (normalized with maximum temperature) respect to non dimensional curvilinear abscissa is shown in Figure 3.12. Results shown that the application of the innovative

geometry can decrease the temperature of all the part of the vane cooled by the new impingement geometries, located from 60% of the pressure side to 60% of the suction side. It's important to notice how a difference in metal temperatures of 10 or 20 degrees can modify component's life of several hundreds working hours, since temperature level can strongly affects fatigue life of a structure. For obtaining the same massflow of the actual case, it's necessary to increase the impingement pressure ratio β (defined as $\beta = (P_{tot,in} - P_{s,out})/P_{tot,in}$), due to the increased pressure losses generated by the innovative configurations, by less than 1%.

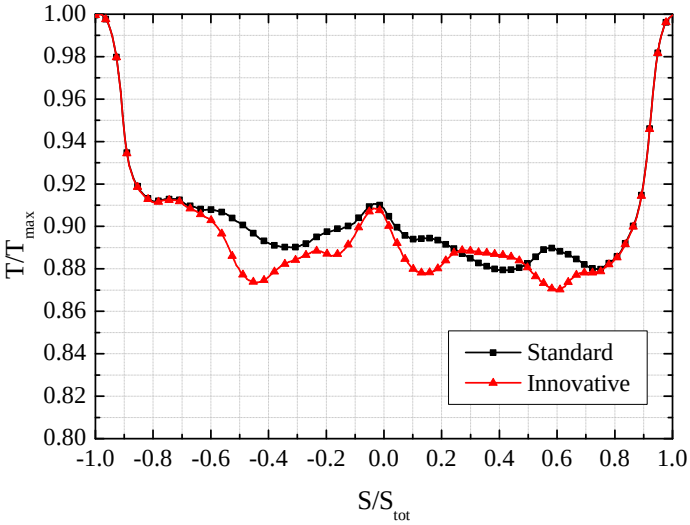

Figure 3.12: Wall temperature results.

3.5 Experimental validation

In the previous paragraphs, innovative impingement geometry have shown good performances compared to a standard one: in this chapter *BLANK CODE* was used for designing a test plate for performing an experimental campaign.

3.5.1 Test rig and measurements description

Experimental tests were performed by the Heat Transfer and Combustion Laboratory of the Department of Industrial Engineering of Florence (DIEF). The test rig (depicted in Figure 3.13) consists of an open-loop wind tunnel, and is designed to replicate, on an enlarged scale, the thermal and fluid-dynamic phenomena involved by impingement array cooling systems; detailed description of the rig and experimental procedure are reported in [112]. The rig presents a modular design, allowing a fast and simple modification of the cooling geometry.

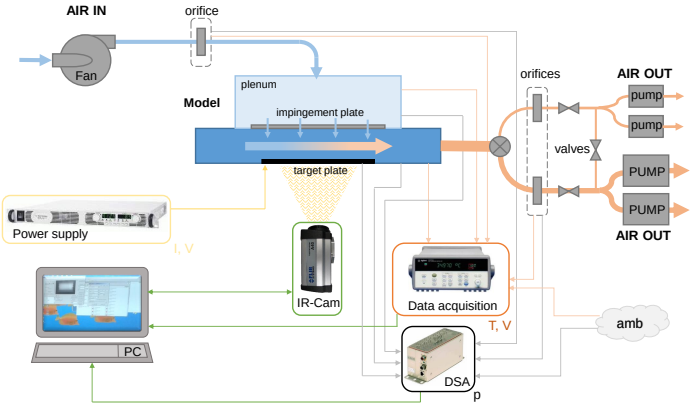

Figure 3.13: Test rig scheme, [112].

Impingement target plate temperature is measured through a *FLIR A40M* IR camera, and a detailed view of the plate is depicted in Figure 3.14; only the external temperature can be directly measured through the camera due to test rig configuration, and as a consequence, the internal plate temperature (on the side of impingement jets) must be indirectly determined. In particular, given the high thermal conductivity and the small but not negligible thickness of the steel support, a simple monodimensional approach was not suitable for the present case, since the conductive heat fluxes parallel to the plate have the same magnitude

of the normal ones: for that reason impingement plate is modeled and analyzed through a finite difference explicit model [112]. Heating power q_{joule} shown in Figure 3.14 was given to the plate by controlling voltage and current intensity.

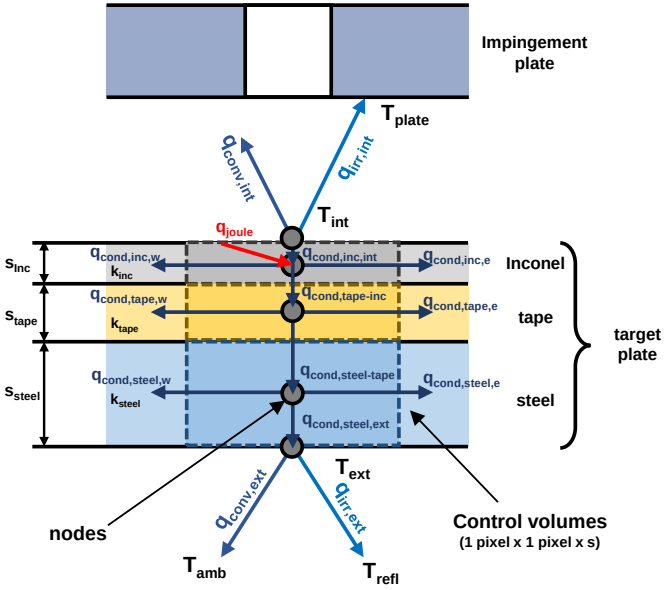

Figure 3.14: Target plate scheme and heat fluxes involved, [112].

3.5.2 Test plate description

The innovative impingement plate designed with *BLANK CODE* has a staggered pattern and all the geometrical characteristics are reported in Table 3.4. For economical and practical reasons, the tested innovative impingement plate is realized with standard manufacturing methods in three pieces, but obviously it could have been realized with DMLS technique. A scheme of the drawing used for plate manufacturing is reported in Figure 3.15, where the three different pieces are clearly visible, while in Figure 3.16 the realized plate is shown. Since *BLANK CODE*

procedure evaluates HTC of impingement by using Florschuetz correlation [39], all the significant parameters were chosen inside the correlation's range of application.

Zone	Diameter [mm]	Spanwise Holes	Streamwise Holes	X/D	Y/D	Z/D
A	3.6	$10-9$	5	3.61	4	2.78
B	3.6	$10-9$	5	4.00	4	2.78
C	3.6	$10-9$	5	3.89	4	2.78

Table 3.4: Innovative impingement plate geometrical parameters.

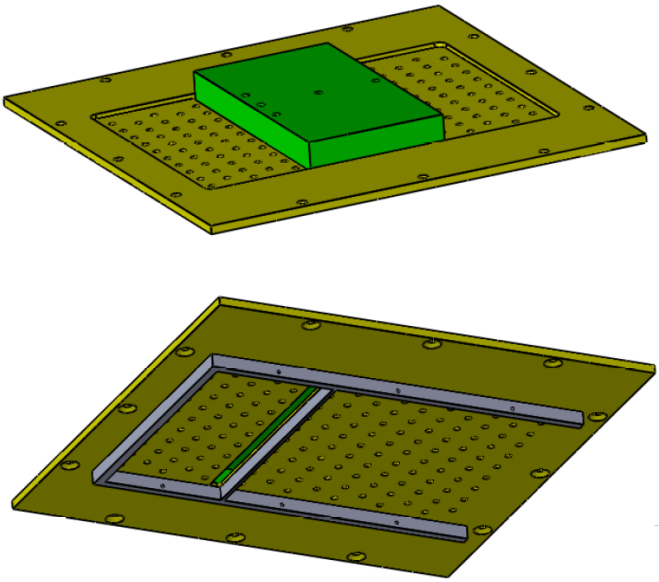

Figure 3.15: Drawings for impingement plate manufacturing.

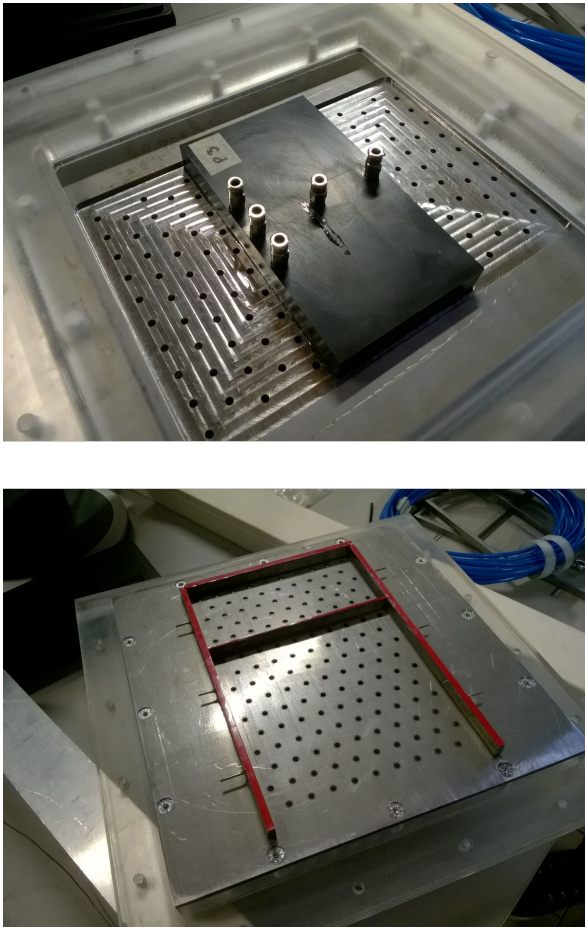

Figure 3.16: Realized impingement plate.

3.5.3 Experimental and *BLANK CODE* results

Experimental procedure developed by Tarchi et al. [112] described in previous chapters allows to evaluate both heat transfer coefficient and metal temperature distribution on the impingement plate. Since *BLANK CODE* was used to design the newly developed impingement plate, a comparison was performed, using the simplified procedure depicted in Figure 3.6. In the experimental campaign external temperature was acquired by IR camera, while HTC and internal temperature were calculated with post-processing; *BLANK CODE* instead allows to acquire HTC data using Florschuetz correlation [39] while internal and external temperatures are obtained at the end of CHT analysis.

In *BLANK CODE* three-dimensional FEM was performed by imposing into the *inconel* plate the same Joule power applied during the experiment, and fluid network was modeled by using specific models that simulated pressure losses between the first two plate zones (two consecutive 90-degrees bends). Discharge coefficient of all the impingement rows were evaluated with a specific CFD simulation, for having a much more detailed flow-field description.

Results of internal temperature distribution obtained by experimental tests and *BLANK CODE* procedure are reported in Figure 3.17, where error bars of 3% are applied on experimental data, as stated in [112]. Results of *BLANK CODE* procedure are really close to the experimental ones and some differences are present just between part A and part B and between part B and part C, where, despite the use of specific pressure losses models, the fluid can not been considered mono-dimensional and strong 3D phenomena are involved.

Figure 3.17 shows how the use of the simplified version of *BLANK CODE* can be a powerful tool for the design of both existent and innovative gas turbine cooling systems.

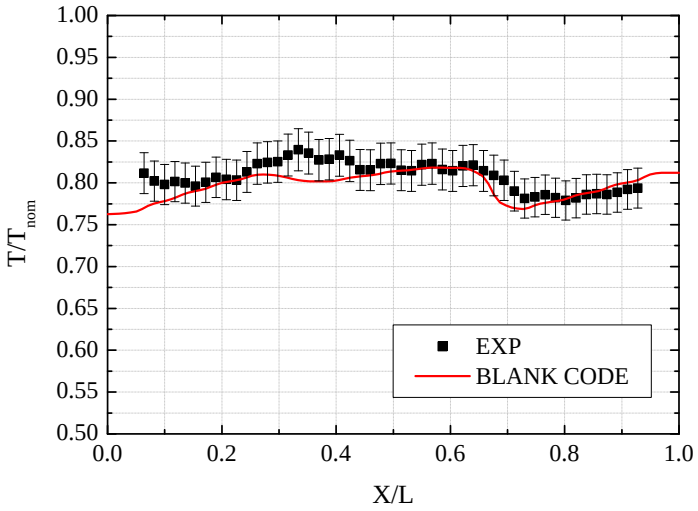

Figure 3.17: Experimental results compared with BLANK CODE.

Chapter 4

Innovative film cooling

In this chapter an innovative geometry for a film cooling shaped hole is presented, whose form could not be obtained with conventional manufacturing procedures (chip removal or EDM). After a geometry description, it has been decided to perform a DoE-type study with the aim of finding an optimal shape in terms of adiabatic effectiveness. This means therefore that equal values of η_{aw} (1.13) could be achieved with a lower mass flow rate of coolant or, in other words, that with equal mass flow rates it's possible to obtain higher η_{aw} values.

4.1 Geometry description

The proposed film cooling hole for gas turbine applications has a high inlet angle α, which guarantee low pressure losses, and a lower exit angle β aimed to maintain the flow attached to the wall. This is possible due to the particular geometry of the hole that guarantee two different angles, taking advantages of both the configurations. Detailed description of geometry and figures can not be reported in this thesis due to a patent pending process; a schematic representation of hole's design (slightly modified for the reasons explained before) is shown in Figure 4.1. Hole geometry guarantee a smooth passages of the flow, avoiding high value of pressure losses due to sudden passage area variations, typical in shaped

holes.

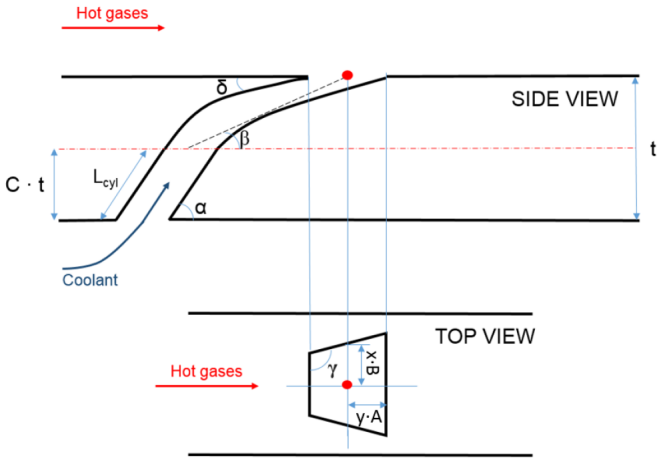

Figure 4.1: Schematic representation of the hole's baseline design.

Dimensions of inlet section were chosen to obtain, on the plane normal to the joining direction, a circular section with a known imposed nominal diameter D. Trapezoidal trace dimensions' were parametrized using A and B: the first parameter has the effect of stretching the quadrilateral in streamwise direction, whereas the second operates a stretching in spanwise direction. The position of the plane where the second trace is located, is defined by the parameter C, that multiply plate thickness t. Opening angle of the trapezoid γ was chosen with a value typical for shaped holes, while another important parameter to be kept under observation is the angle δ formed between the plate and the upstream side of the hole, near the exit. This angle should not be less than a certain value because the upper surface can collapse on the hole during manufacturing process. A list of all the fixed and variable parameters is reported in Table 4.1. It's important to notice that δ is dependent from other parameters, like α, β and C.

Parameter	Symbol	Value
Nominal hole diameter	D	Fixed
Plate thickness	t	Fixed
Opening angle of the trapezoid	γ	Fixed
Trapezoid streamwise stretching factor	A	Variable
Trapezoid spanwise stretching factor	B	Variable
MID plane position	C	Variable
Tilt of the first part of the hole	α	Variable
Tilt of the second part of the hole	β	Variable
Upper plate angle	δ	Dependent

Table 4.1: Geometric parameters characterizing film cooling hole.

4.2 Geometry optimization

Since a lot of parameter are involved in defining hole's geometry, an optimization is necessary, where a certain number of goals (even in contrast with each other) have to be simultaneously achieved.

For a long time industries have been adopted the classical process to optimize the design of new components: development of a CAD model with a baseline design, CFD (or global numerical simulation), analysis of the results and final evaluation of its performance. This kind of procedure can presents several drawbacks, for example if at the end of post-processing the results do not meet the criteria, cycle has to be restarted from the beginning with a new modified CAD (Figure 4.2a) but the real problem is to understand how to change the geometry of the component to match all of the objectives and eventual project constraints.

The idea behind an optimization based on a *DoE* (Design of Experiments) is to build a response surface from which provide quickly the approximated values of the output parameters, everywhere in the analyzed design space, without having to perform a complete solution. The advantages are represented by a considerable time saving during numerical simulations and by a purely goal driven optimization, thank to the informations extracted from the response surfaces. DoE, in order to

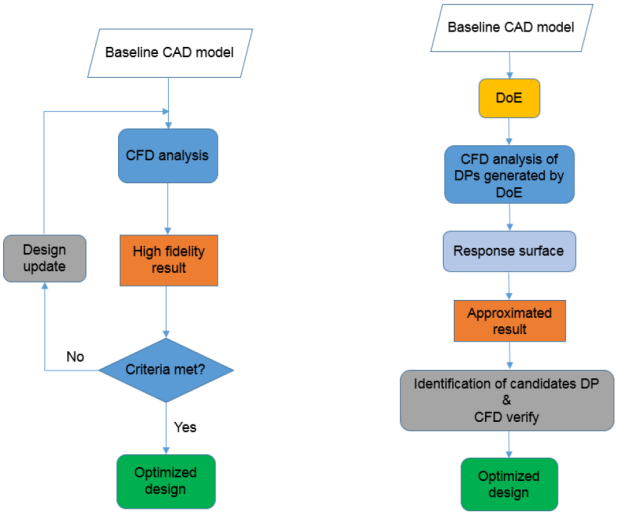

Figure 4.2: Flow charts that illustrate two different ways to achieve an optimized design: without DoE (a) and with DoE (b), [113].

build response surface, combines the input parameters to obtain a set of Design Points (DP) and then performs a CFD analysis for each of them. This set has to cover properly all the design space; the way with which DP are chosen depends on the specific algorithm selected for the DoE. Starting from the response surface, with a Pareto-type analysis, is then possible to individuate some candidate points among all the design points which better satisfy goals and constraints. A CFD analysis could now be performed to validate the approximated result of the most promising DP, following the diagram reported in Figure 4.2b.

DoE analysis is carried out with *ANSYS Workbench*® DoE module linked to other modules using specific parameters. *ANSYS Fluent*® is used for CFD simulations while CAD and numerical grid are generated automatically by using *ANSYS Design Modeler*® and *ANSYS Meshing*® respectively; post process is performed using *ANSYS CFX-Post*® .

The automated process inside *ANSYS Workbench®* environment is depicted in Figure 4.3. CFD simulations setup had been previously validated ([113]) on literature test cases, like Sinha et al. [114] and Pietrzyk [115].

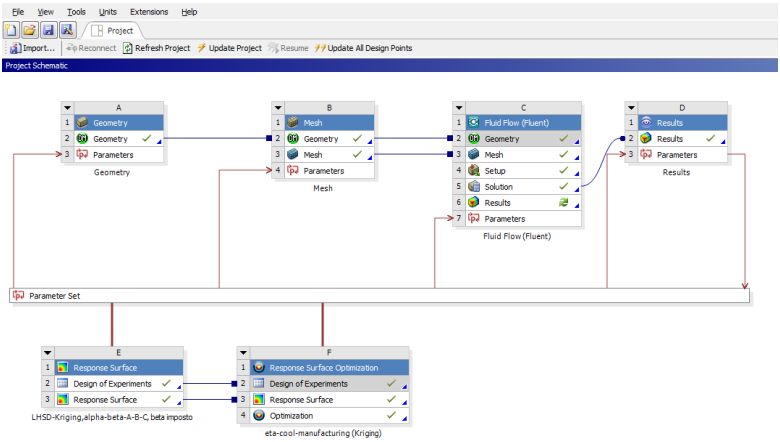

Figure 4.3: ANSYS Workbench® environment for DoE and optimization; all the used modules are shown.

4.2.1 Numerical DoE setup

The set of the design points generated is closely related to the number of parameters that can vary during the DoE study and to the scheme used by the software to combine these parameters each other. In this work fluid dynamic conditions are fixed (pressure drop seen by the hole and density ratio) to investigate only the influence of the geometrical parameters on cooling performances. In particular five of them were varied in this study: α, β, A, B and C (for details refer to Table 4.1). For each parameter an upper and a lower limit values were fixed, in order to avoid cases where the trapezoid could exit laterally from the domain (modifying A and B), while α is fixed always greater than β and C not over half of the plate thickness.

Several types of Design of Experiments are available in *ANSYS Workbench*® such as the Latin Hypercube Sampling design (LHS). With its algorithm the points are randomly generated in a square grid across the design space, but no points can share the same value. However, the DoE type chosen for our study is the Optimal Space-Filling design (OSF), which is a model initialized as an LHS and then optimized several times, remaining a valid LHS (without points sharing rows or columns) while achieving a more uniform space distribution of points, maximizing the distance between them. Essentially OSF is able to distribute the design parameters equally throughout the design space with the objective of gaining the maximum insight into the design with the fewest number of points [116]. Numerical results obtained from the 50 RANS simulations (performed with $k-\omega$ SST turbulence model), one for each DP, will be then used to build the response surface, from which extract the approximated solutions and then drive the final optimization stage.

4.2.2 Numerical DoE results

Response surface, build using *Kriging* method [116], allows to understand the influence of each parameter on the global solution. In Figure 4.4 the influence of α and β angles on coefficient of discharge (Figure 4.4a) and adiabatic effectiveness (Figure 4.4b) spanwise averaged on a $10D$ length surface are shown. It's important to notice that simulations are performed imposing pressure ratio, and that increasing α and decreasing β it's possible to reach higher η_{aw} value but with higher massflow consumption. Since five parameters are changing and the influence of each one on adiabatic effectiveness and mass flow is not easily predictable, on automatic optimization is necessary.

A MOGA optimization (Multi Objective Genetic Algorithm) was conducted in order to find 3 optimal design configurations by fixing two goals:

- Maximize adiabatic effectiveness;
- minimize massflow consumption.

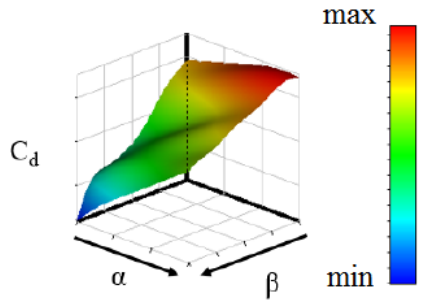

(a) Influence of α and β on Cd.

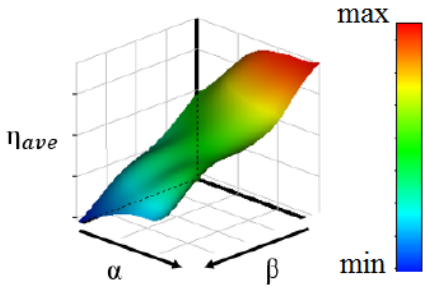

(b) Influence of α and β on η_{aw}.

Figure 4.4: Influence of α and β on Cd and η_{aw}, fixing A, B and C parameter.

and a constraint:

- maintain δ angle under a specific value.

Once three optimal candidate points were found and verified through CFD simulations [113], the most promising one was chosen for performing experimental test, exploited in the next paragraph. Chosen design point have a high value of α and a low β, but not equal respectively from the maximum and minimum value, while the trapezoid outlet section is maintained as larger as possible.

4.3 Experimental campaign

Adiabatic effectiveness measurements for innovative film cooling holes have been performed by using Pressure Sensitive Paint (PSP) technique; experimental apparatus is now described.

4.3.1 Test rig description

Experimental tests were carried out by THT Lab (laboratory of Technology for High Temperature) of the Department of Industrial Engineering of Florence (DIEF), using a test rig, depicted in Figure 4.5, with a constant cross section area (120x40 mm^2) crossed by the mainstream, drawn by means of two vacuum pumps from the ambient. Before entering into the test section, mainstream flows through an honeycomb and several screens to set a uniform velocity profile; mass flow rate is measured with an orifice, placed downstream of the test rig, according to the standard EN ISO 5167-1. This experimental campaign was conducted without turbulence generator, maintaining Tu level of 1 %. Film cooling holes are fed by a plenum chamber where honeycomb and screens are present. Coolant flow is provided by tanks with technical gas: in the present study pure N_2 and $SF_6 + N_2$ mixture was used to perform adiabatic effectiveness measurements. These gas mixture allows to achieve respectively DR equal to 1.0 and 2.5. Flow rate is set up by a dedicated valve and measured with a Coriolis flowmeter located on the cooling line.

Scanner *Scanivalve DSA 3217* with temperature compensated piezoresistive relative pressure sensors measure the static pressure in 9 different locations with a maximum uncertainty of ± 17 Pa, while T type thermocouples (uncertainty ± 0.5 K) connected to a data acquisition/switch unit (*HP/Agilent 34970A*) measure the mainstream temperature. An high performance UV LED Illuminator system *IL104* provide the adequate light source for the PSP surface excitation, while a 1600x1200 resolution 14-bit CCD camera (*PCO.1600*) with a 610 nm red filter records the intensity emitted by PSP.

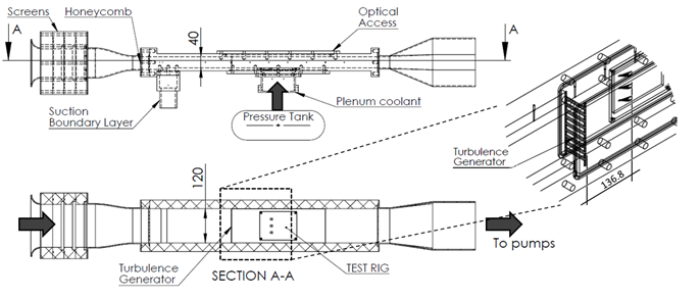

Figure 4.5: Schematic representation of test rig.

4.3.2 Adiabatic effectiveness measurements

Pressure sensitive paint (PSP) is an organic substance, composed by oxygen sensitive molecules embedded in the paint solution using a polymer binder permeable to oxygen. Through the exploitation of the luminescence behavior of these molecules, PSP can be used to measure oxygen concentration of the atmosphere surrounding the paints, which in turn can be linked to the partial pressure of air. This property makes the paint suitable for gas concentration technique based on the heat and mass transfer analogy, e.g. for adiabatic effectiveness measurements [117]. Assuming valid the analogy, if a tracer gas without free oxygen (e.g. N_2 or CO_2) is used as coolant, it's possible to replace definition of film cooling effectiveness in terms of O_2 partial pressure measured by PSP:

$$\eta_{aw} = \frac{T_{gas} - T_{aw}}{T_{gas} - T_{cool}} \equiv \frac{C_{gas} - C_w}{C_{gas}} \tag{4.1}$$

where C_{gas} and C_w are oxygen concentrations, respectively, in the main free stream and in proximity of the wall. More details on PSP measurements for GT applications can be found in works of Navarra [118], Caciolli et al. [119] and Andreini et al. [120].

4.3.3 Test plate manufacturing

Experimental test plate was designed by scaling the film cooling holes (3 holes were placed into the plate for having a uniform test and assure repeatability) of a factor 3 : 1 in order to reach Reynolds number typical of gas turbine application inside holes. Test plate was then printed using *Polyjet* technique [121] with an *Objet Eden 260®* printer; material used is *VERODENT MED670* [122]. Polyjet technique consists on a layer-by-layer polymer deposition: after each layer is deposed, it's immediately hardened by UV light emitted by specific UV lamps. Loose powder or a second jet with gel material can be used for supporting the part during the process. More details about polyjet, whose process is shown in Figure 4.6, or additive manufacturing technique can be found in [121], while the 3-D printed plate is reported in Figure 4.7.

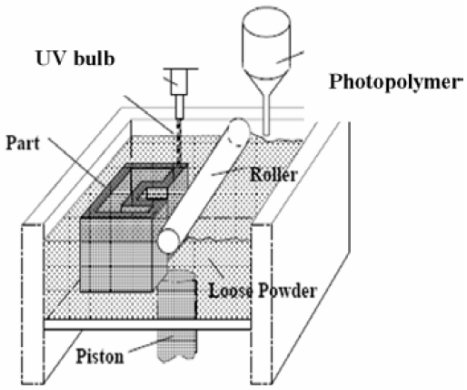

Figure 4.6: Polyjet process scheme, [121].

4.3.4 Experimental results

Results of experimental campaign using test matrix reported in Table 4.2 are now shown in terms of adiabatic effectiveness maps and spanwise averaged (over one pitch) plots.

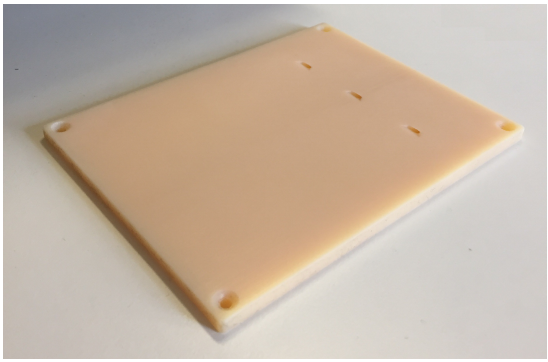

Figure 4.7: 3-D printed test plate.

DR [-]	*BR [-]*				
1.0	0.50	0.75	1.00	1.25	1.50
2.5	0.50	0.75	1.00	1.25	1.50

Table 4.2: Test matrix of innovative FC hole's experimental campaign.

In Figure 4.8 two-dimensional adiabatic effectiveness maps, with a dimension of 50 nominal diameter length and 1 spanwise pitch height, are reported for all test matrix points. Central hole, unaffected by boundary effects, is chosen. Maps in Figure 4.8 show an increase with BR and DR, as expected from film cooling theory [17, 45]; it can be also noticed how coolant coverage continue over $40D$ downstream hole exit, even in the worst condition ($BR = 0.50$, $DR = 1.0$). All tests show a slight non symmetric distribution of cooling respect to the centerline, maybe generated from some irregularity inside the hole generated during manufacturing.

Spanwise averaged (over 1 pitch) adiabatic effectiveness distribution over X/D (where X is axial abscissa and D is the nominal diameter) are reported in Figure 4.9 for both studied DR values: increasing behavior with BR augmentation and the extended coverage of the innovative hole over $40D$ can be appreciated. Comparing the results of two analyzed density ratios an increase of 25% can be appreciated near hole's exit.

4.3.5 Comparisons with literature correlation *(BANKS)*

Innovative film cooling hole was then simulated with *BANKS* imposing the same discharge coefficient found by experimental tests. Results in terms of massflow (*BANKS* simulation were performed by imposing total pressure at the inlet and static pressure at the outlet) shows an error of less then 1% respect to experimental tests, for all conditions. Adiabatic effectiveness correlation used for evaluating hole performance is the one developed by Colban, Thole and Bogard on shaped film cooling holes [52]. This correlation, shown in 4.2, characterize performances of film cooling holes with a shape like the one shown in Figure 4.10. Geometrical parameters that influence $\bar{\eta}$ are t, P (referring to Figure 4.10) and non dimensional value ξ (4.3) that depends itself from nominal diameter D, axial position X, spanwise pitch P, BR and AR defined as the ratio between A_{exit} and A_{in}. Numerical values of C_1, C_2 and C_3 and details about the meaning of ξ parameter can be found in [52]. Innovative hole described in Chapter 4.1 is quite different from holes that were used for developing 4.2 correlation but at the same time is similar to a shape like the one depicted in Figure 4.10 and it can be notice how main parameters influencing $\bar{\eta}$ like t, BR, P and area ratio AR can be easily calculated also for innovative hole and it can be expected that they modify film cooling coverage in a similar way.

$$\bar{\eta} = \frac{1}{{}^{P}/_{t} + C_1\, BR^{C_2}\, \xi^{C_3}} \tag{4.2}$$

$$\xi = \frac{4}{\pi} \frac{{}^{X}/_{D}\ {}^{P}/_{D}}{BR \cdot AR} \tag{4.3}$$

Authors in [52] define their correlation using a dataset that have a constant value of α and DR values typical of gas turbine applications ($1.7 \div 2.0$) and for that reason these parameters are not included into Eq. 4.2 ([52]). Experimental tests were performed by using two different density ratios (1.0 and 2.5) and α in innovative geometry it's not too far from the value used in [52]: for these reasons in Figure 4.11 experimental

tests are compared with *BANKS* simulations for different BR. Results in Figure 4.11 show how the density ratio improve film cooling coverage, especially for higher blowing ratios. Comparisons with *BANKS* using a correlative approach show a quite high error near hole's exit, due to different geometry and by consequence a different hole behavior of the analyzed case with a shaped hole; considering results from 5 to 40 nominal diameters difference from experimental tests are variable from more than 25% to less than 9%. These discrepancies are not that high considering different conditions and different geometry for which the used correlation were developed, and results show how a run performed with *BANKS* can be useful to characterize the performance of a new geometry with an existing correlation found in literature. An extensive experimental (or numerical) campaign changing geometry and fluid dynamic conditions can be performed in order to find parameter that correct the existing correlation or develop a new one, that can be easily implemented into *BANKS* subroutines.

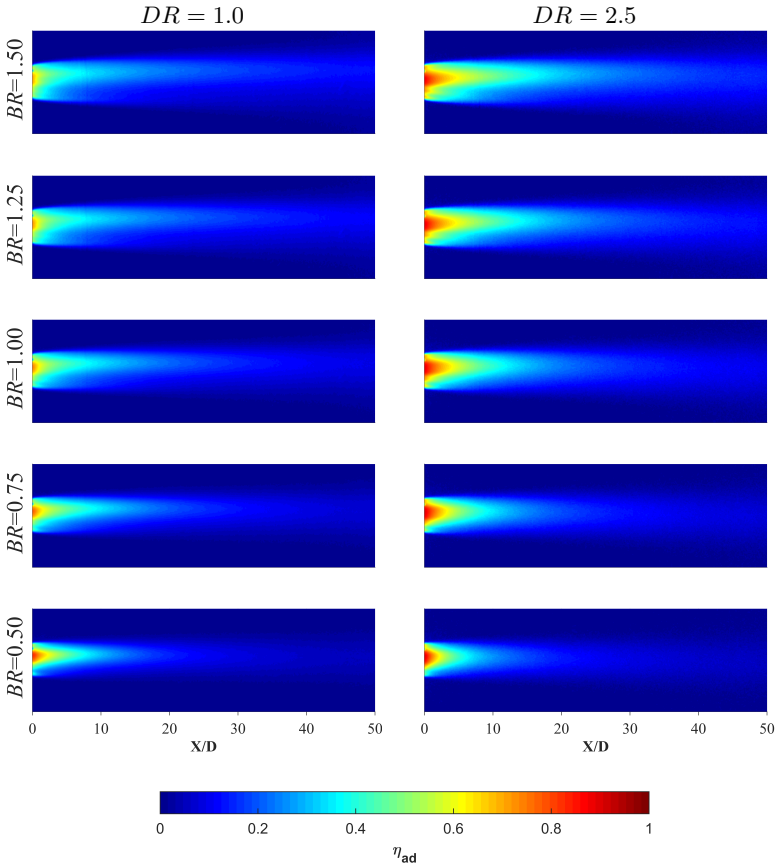

Figure 4.8: 2D maps of adiabatic effectiveness of all test points described in Table 4.2.

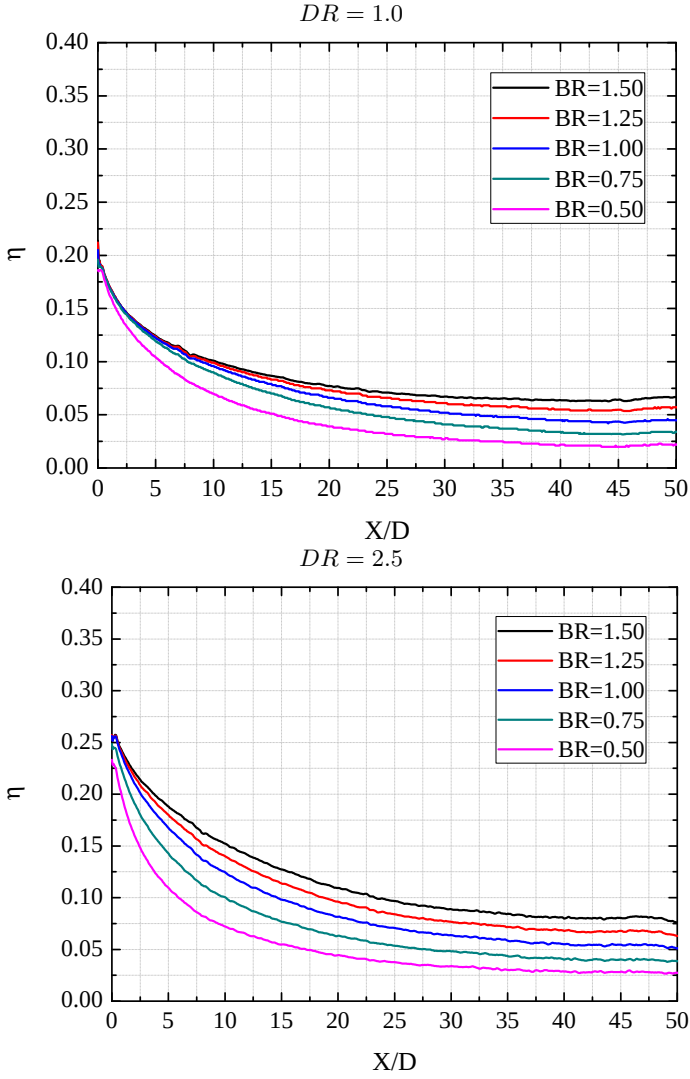

Figure 4.9: Spanwise averaged adiabatic effectiveness distribution.

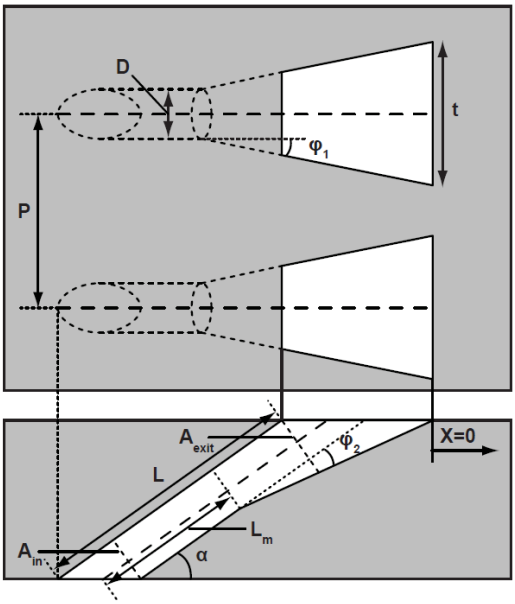

Figure 4.10: Shaped hole geometrical parameters.

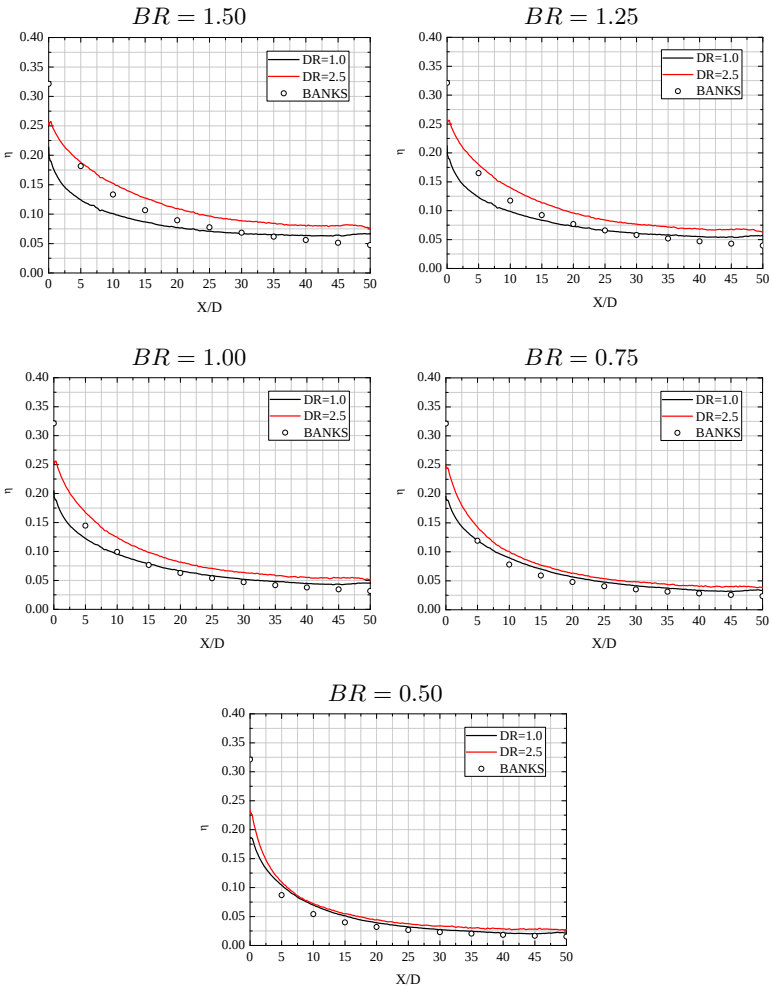

Figure 4.11: Spanwise averaged (over 1 pitch) adiabatic effectiveness at the two different density ratios for all BR, compared with [52].

4.3.6 Comparisons with CFD simulations

RANS CFD simulations were carried out for having additional comparisons with experimental data. Since experiments described in section 4.3 are conducted without temperature difference, numerical simulations too are carried out in the same conditions: for that reason, in order to track the coolant distribution, since adiabatic effectiveness can not be defined (see Eq. 1.13), a transport equation for an additional passive scalar representing coolant concentration, holding the value 1 at the coolant inlet and 0 at the mainstream inlet, was solved. The value of its kinematic diffusivity was specified to guarantee a $Le = 1$ with the aim of fully respecting the mass-energy transfer analogy [123]. Numerical setup and domain are the same described in section 4.2. Figure 4.12 shows spanwise averaged adiabatic effectiveness results for $BR = 1.50$, $BR = 1.00$ and $BR = 0.50$, all for $DR = 1.0$.

Results shows that adiabatic effectiveness evaluated by CFD are higher then both experimental and correlative results. It's well known that film cooling problems are not easily solved by steady RANS simulations, but in this case the discrepancies between CFD and experimental results can be justified also by the different pressure ratio evaluated by the CFD respect to the one measured by the experimental campaign. CFD simulations, carried out imposing experimental measured massflow at the inlets and static pressure at the outlet, showed a pressure ratio of 6.5%, 3.2% and 0.9% lower respect to the experiments, for $BR = 1.50$, $BR = 1.00$ and $BR = 0.50$ cases respectively. These differences can be related to some irregularities inside the hole (that can justify also the non symmetric behavior shown in the maps of Figure 4.8) that increase the roughness of hole's surfaces: a high wall roughness can in fact justify the pressure losses increasing with the increasing velocity. Unfortunately it's not easy to determine wall roughness value, since its value is dependent from 3-D technique used and build direction [67, 68, 124].

In conclusion neither the existing correlation available in *BANKS* nor a RANS simulation can perfectly match the experiments, but uncertainties are present both in the experimental and numerical results. Figure 4.12

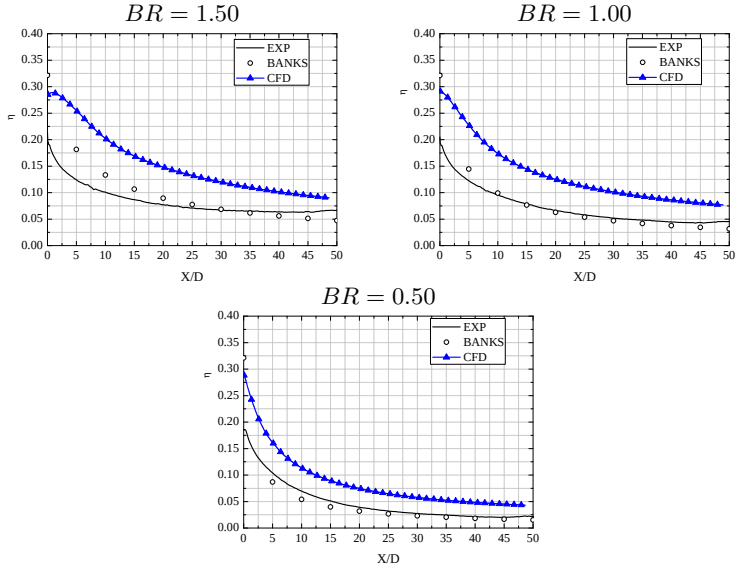

Figure 4.12: Adiabatic effectiveness distribution for $BR = 1.50$, $BR = 1.00$, and $BR = 0.50$ for $DR = 1.0$: comparison between experiments, BANKS and CFD.

show that the newly developed film cooling hole has a similar behavior to the results evaluated with Colban et al [52] correlation, developed for shaped holes, but numerical RANS simulations indicate that maybe experimental test plate can be characterized by some differences respect to the perfect geometry simulated in CFD, like the presence of a high wall roughness inside the film cooling hole. Despite these differences in results, numerical simulations show a similar behavior of η distribution for all the tested BR, validating the optimization process carried out for finding the best geometrical parameters.

Future developments can consider an accurate analysis of the effective geometry realized with polyjet by using CT scan ([67]), developing a model for finding an equivalent roughness to be applied in CFD, and realize the plate with different additive manufacturing techniques.

Conclusions

Gas turbine components have reached a high level of development due to the wide use of these kind of engine both in power generation and aeronautical propulsion. During design phase of gas turbine components, it has therefore become essential to develop methods for predicting metal temperature distribution in order to analyze thermal stresses and lifespan. Numerical methods like CFD Conjugate Heat Tranfer (CHT) analyses, represents a fundamental tool in order to model and study gas turbine components, but can be time consuming. A powerful design tool can be the key to successfully achieve industrial requirements in a short amount of time.

This work deals with a numerical method to estimate the temperature status of gas turbine endwalls, blades, and nozzles, developed in collaboration with *GE Oil & Gas Nuovo Pignone*® , solving the involved domains in a decoupled way; each field of the problem is resolved with a different approach: a simplified 3D CFD without accounting film cooling holes is used to evaluate hot gas path, a 3D FEM provides the conductive solution, while a 1D fluid network based on literature correlations is used to model cooling flows. The use of a mono-dimensional solver and no need to mesh the cooling features allows to speed up the solution, while the decoupled nature of the procedure permits to perform sensitivity analyses in a short time. Several numerical tools are developed for fluid network creation, for linking the three-dimensional with the mono-dimensional domain and in general for shortening the solution time of the proposed procedure, called *BLANK CODE*. Two literature test cases, representing vanes with

different cooling configurations, are used for validating *BLANK CODE*; results are compared in terms of available experimental data, in particular airfoil static pressure and metal temperature distributions. Comparisons showed a very good agreements in both configurations (with and without the presence of film cooling rows) and main errors seems to be related to 3D CFD modeling and its inabilities to catch transition point, but in general metal temperature distribution behavior and values are well solved. This validation phase showed the capabilities of *BLANK CODE* in verifying an existent cooled blade starting from hot gas path and internal cavities boundary conditions.

After that the strength of the procedure was verified, it was used as a design tool for the improvement of an innovative concept of impingement cooling. The proposed geometry had the goal to limit the detrimental effect of impingement crossflow in the cooling performance, by interrupting it after a certain number of rows. After that a comparison between a complete CFD CHT calculation and *BLANK CODE* showed only little differences in the solution despite a remarkable saving in computational time, the procedure was used to perform several simulations in order to find the driving parameters for geometry improvements. The modified configuration allowed to obtain a uniform lower temperature distribution with just a little increase in pressure drop. Innovative concept was applied also to a second stage vane characterized by a large array of impingement cooling rows generating high crossflow near the trailing edge: the new configuration confirmed a decrease in metal temperature values with a little increase in pressure losses. The decoupled procedure was then used for designing an innovative plate for a test rig: results of experimental campaign were compared with *BLANK CODE* with very good agreements. The procedure showed a good ability to predict gas turbine components metal temperatures, in particular for performing fast comparisons between different geometries or to carry out sensitivity analyses.

A novel concept of film cooling holes is then presented in this work. Since the use of additive manufacturing techniques are becoming a trend in industrial procedures, both the previously presented impingement

cooling than this novel hole are designed without the constraints imposed by classic manufacturing procedures like EDM, chip removal or milling. The new concept for film cooling hole is mainly based on having two different angles: a higher one for limiting entrance effect losses, and a lower one at the exit, for maintaining as much coolant as possible attached to blade surface. Outlet area is trapezoidal shaped, like classical *shaped holes*. A numerical optimization analysis was performed in order to find optimal values for the geometrical parameters involved; the most promising geometry was then realized with a 3D *polyjet* printing, showing its manufacturability. An experimental test campaign was carried out in order to understand hole performance. Results were compared with simulation conducted with *BANKS*, *BLANK CODE*'s network solver, that implements correlation for evaluating film cooling performances. In particular a correlation for shaped holes was used, because it depends only by fluid dynamic conditions, trapezoid dimensions and outlet/inlet area ratio, letting it reliable also for the novel concept. Comparisons, also with numerical RANS simulations, showed that the newly developed film cooling hole act in a similar way to a shaped hole, with higher η values if compared with *BANKS* correlation. Experimental results showed lower values respect to CFD, to be assured at a high wall roughness generated inside the hole.

A design procedure and two innovative cooling concepts are presented in this work, with the goal of decreasing the design-to-production time while increasing thermal cooling performance, allowing a global increase in gas turbine engine cycle efficiency.

Appendix A

Hot side heat transfer evaluation in *BLANK CODE* procedure

Heat transfer coefficient evaluation in the iterative procedure presented in Chapter 2.1 are retrieved at every iteration using a 3D CFD analysis imposing wall temperature coming from the most updated FEM results, using following equation:

$$HTC_{ext} = \frac{\dot{q}}{(T_{aw} - T_w)} \tag{A.1}$$

where $\dot{q}$ is the heat flux, T_w is the wall temperature from the last simulation, and T_{aw} is the adiabatic wall temperature, evaluated only at the beginning of the procedure. Since the presented numerical methodology had to be a fast design tool, it's obvious that performing a 3D CFD at every iteration can be time consuming respect to the computational time spent by other solvers (fluid network and FEM). For that reason two alternative way for evaluating external heat transfer coefficient were developed: the first one, called *3 points approach*, needs 4 total CFD simulations, and an analytical correlation for linking HTC and wall temperature, while the second one, called *Two run approach*, needs only 2 CFD simulation and HTC it's not considered temperature-dependent.

A.1 3 points approach

The first methodology presented for evaluating HTC considering its dependence with wall temperature, it's based on the correlative approach presented by Maffulli and He [92]. In their paper, authors underline the strong dependence that TR (temperature ratio, $TR = T_w/T_{0in}$) could have on HTC distribution by using CFD simulations, as reported in Figure A.1.

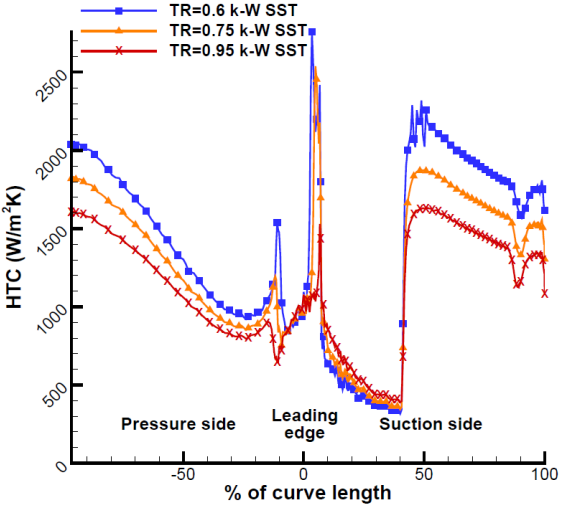

Figure A.1: Dependency of external HTC distribution on the wall temperature ratio using $k-\omega$ SST turbulence model, [92].

Authors in [92] stated that the non-linear behavior of the heat flux respect to wall temperature can be described by a non-linear equation:

$$\dot{q} = C_1 + T_w\, C_2 + T_w^2\, C_3 \tag{A.2}$$

Values of three coefficients C_i can be found by solving a linear system

using available data for three imposed temperature simulation. Goodness of solution is shown in Figure A.2; this method is validated also with 3D calculations [93].

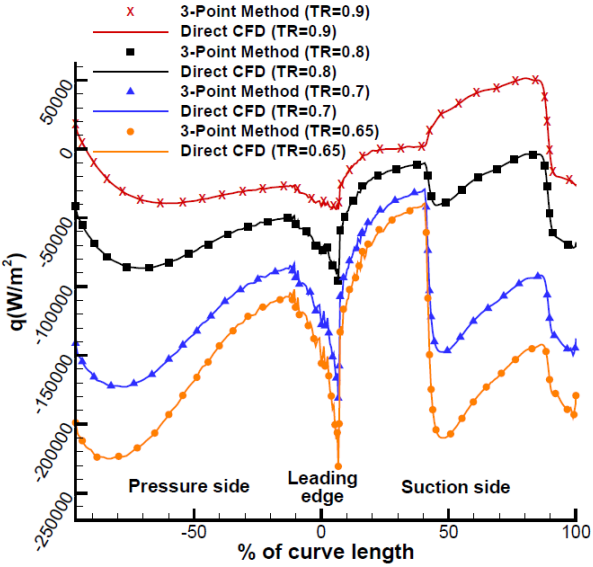

Figure A.2: Heat flux comparison between the direct cfd solutions and those constructed from the 3-points model, [92].

For implementing this approach in *BLANK CODE* procedure, it's necessary to perform 3 imposed wall temperature simulations for finding C_i coefficients and an adiabatic simulation for finding T_{aw}. Before starting the iterative procedure, C_i coefficients had to be found for all numerical grid points and stored into a file, that will be used for finding $\dot{q}$ values (with Equation A.2) after every FEM solution. If 3 points approach it's used, iterative procedure change from Figure A.3a to Figure A.3b.

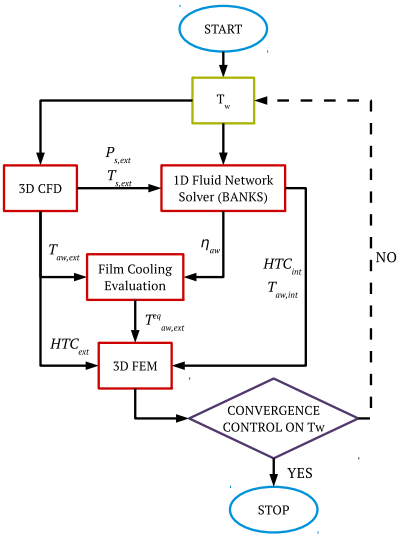

(a) Standard procedure.

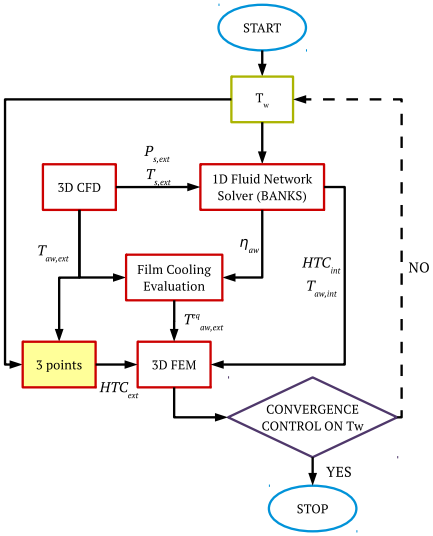

(b) Modified procedure.

Figure A.3: Iterative procedure modification by using 3 points approach.

A.2 Two run approach

A more simplified approach is to perform just two CFD simulations: an adiabatic and a fixed temperature. Fixed temperature simulation is performed by imposing (on the surface where we want to evaluate heat transfer) a temperature distribution equal to the adiabatic one scaled with a fixed value in a way that temperature difference is always constant:

$$HTC_{ext} = \frac{\dot{q}}{(T_{aw} - T_w)} = \frac{\dot{q}}{\Delta T_{fix}} \tag{A.3}$$

Applying two run approach allows to strongly reduce computational time and the iterative procedure it's modified as reported in Figure A.4.

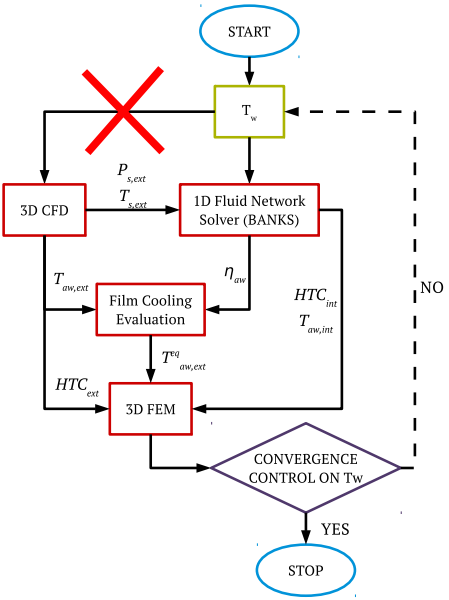

Figure A.4: Iterative procedure modification by using 2 run approach.

A.3 Comparisons

3 points and two run approaches are compared in order to assure their equality. All the comparisons are performed using test case described in Chapter 2.2.1. First of all HTC is evaluated with 3 different fixed temperature values (and so different TR), using Equation A.1, and results seem to be influenced by temperature values, as reported in Figure A.5. These three simulations were then used to calculate C_i coefficients for 3points method.

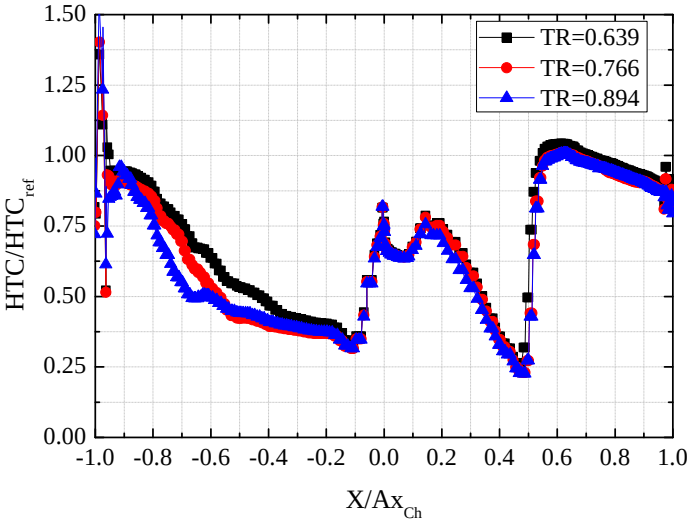

Figure A.5: Heat transfer coefficient comparison by using 3 different temperature ratios.

Heat transfer coefficient comparison for 3 points method (evaluated with most updated temperature distribution) and two run approach is reported in Figure A.6, while correspondent airfoil metal temperature distribution at midspan is reported in Figure A.7. Results show that small differences are present in HTC comparisons and even smaller for T_w, and so the simplest approach can be used. For the analyzed test case, temperature

differences are not so high, and for cases with stronger differences a comparison between results obtained with the two method it's recommended. *Two run* method can be easily used for a design phase, verifying only in the last analysis wall temperature effect with *3 points* approach. It's important to notice that in presence of a lot of film cooling rows, 3 points method can be a wrong choice, because in this case HTC value it's not only influenced by wall temperature but also from film cooling presence.

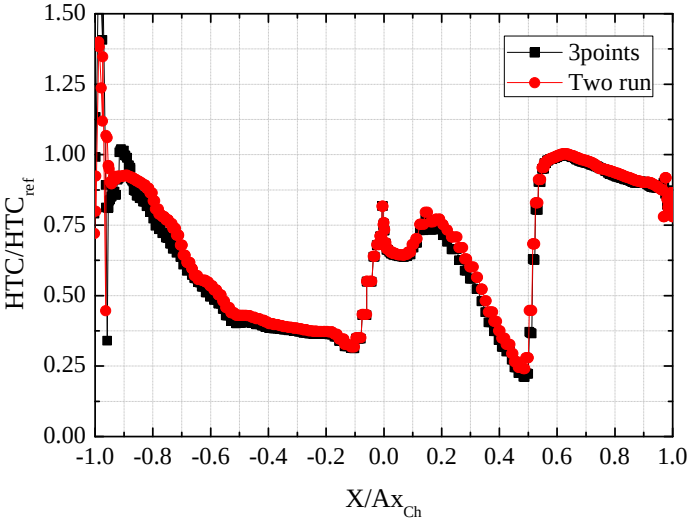

Figure A.6: Heat transfer coefficient comparison by using different approaches.

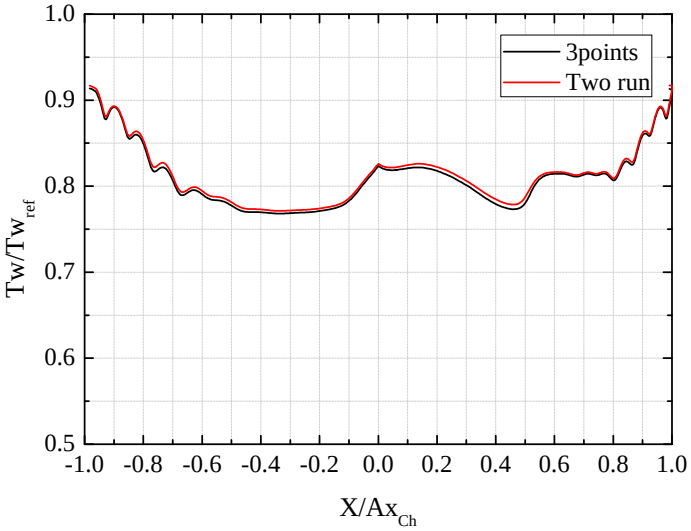

Figure A.7: Wall temperature comparison by using different approaches.

Appendix B

NEST: NEtwork Setup Tool

Since *BANKS* needs a lot of detailed text input files reporting geometrical characteristics, film cooling hole positions and fluid network links between the models, an automatic tool for fluid network setup was developed. This tool, called *NEST* (NEtwork Setup Tool), is written in *Fortran90* and is the link between industrial CAD, Siemens® NX, and *BANKS*. A specific tool written in *C#* is developed by *GE Oil & Gas Nuovo Pignone®* , using available *API* dataset inside the CAD: this application allows to create the entire vane cooling system by using all the features available in *BANKS* and to export *xml* files with all the geometrical informations. *NEST* use these *xml* files as input (open subroutines are implemented as parser [125]) and automatically create all input files required by *BANKS*.

Logical controls and best practices design criteria are implemented for linking elementary models in a representative fluid network.

List of Figures

List of Tables

Bibliography

[1] Moustapha, J., Zelesky, M. F., Baines, N., and Japikse, D. "Axial and radial turbines." *Concepts NREC*, 2003.

[2] Stecco, S. *Impianti di conversione energetica.* Pitagora Editrice Bologna, 1991.

[3] Meece, C. E. "Gas turbine technologies for the future." 12^{th} *Symposium on Air-Breathing Engines*, Vol. 1, 1995.

[4] DeLuca, D. P. and Annis, C. "Fatigue in single crystal nickel superalloys." *Office of Naval Research*, FR21999-23, 1994.

[5] Arakere, N. J. "High-temperature fatigue properties of single crystal superalloys in air and hydrogen." *ASME Paper*, 2001-GT-0585, 2001.

[6] Naik, R. A., DeLuca, D. P., and Shah, D. M. "Critical plane fatigue modeling and characterization of single crystal nickel superalloys." *ASME Journal of Engineering for Gas Turbines and Power*, 126: 391–400, 2004.

[7] Maclachlan, D. W. and Knowles, D. M. "The effect of material on the analysis of single crystal turbine blades: Part I - Material Model." *Fatigue and Fracture Engineering Material Science*, 25: 385–398, 2002.

[8] Maclachlan, D. W. and Knowles, D. M. "The effect of material on the analysis of single crystal turbine blades: Part II - Component

Analysis." *Fatigue and Fracture Engineering Material Science*, 25: 399–409, 2002.

[9] Seetharaman, V. and Cetel, A. D. "Thickness debit in creep properties of PW1484." *Superalloys 2004*, pages 207–214, 2004.

[10] Sims, C. T., Stoloff, N. S., and Hagel, W. C. *Superalloys II: High-Temperature Materials for Aerospace and Industrial Power*. John Wiley & Sons, 1980.

[11] Ballal, D. R. and Zelina, J. "Progress in aeroengine technology (1939-2003)." *Journal of Aircraft*, 41:43–50, 2004.

[12] Bunker, R. S. "Gas turbine heat transfer: 10 remaining hot gas path challenges." *ASME Paper*, GT2006-90002, 2006.

[13] Andreini, A., Bonini, A., Carcasci, C., Facchini, B., Innocenti, L., and Ciani, A. "Conjugate heat transfer calculations on GT rotor blade for industrial applications. Part I: equivalent internal fluid network setup." *ASME Paper*, GT2012-69846, 2012.

[14] Andrei, L., Andreini, A., Facchini, B., and Winchler, L. "An in house developed decoupled procedure: application and validation on a gas turbine vane with different cooling configurations." *Energy Procedia*, 45:1087–1096, 2014.

[15] Torbidoni, L. and Horlock, J. H. "A new method to calculate the coolant requirements of a high temperature gas turbine blade." *ASME Paper*, GT2004-53729, 2004.

[16] Kreith, F., Manglik, R., and Bohn, M. *Principles of Heat Transfer*. Cengage Learning, 2010.

[17] Han, J. C., Dutta, S., and Ekkad, S. *Gas Turbine Heat Transfer and Cooling Technology*. Taylor & Francis, 2000.

[18] Rolls-Royce plc. *The Jet Engine*. Fifth edition, 1996.

[19] Maiuolo, F. *Experimental Analysis of Gas Turbine Airfoil Leading Edge Cooling Systems.* PhD thesis, Università degli Studi di Firenze, Dipartimento di Energetica Sergio Stecco, 2012.

[20] Han, J. C. and Huh, M. "Recent studies in turbine blade internal cooling." *Heat Transfer Research*, 41:803–828, 2010.

[21] Bergman, T. L., Lavine, A. S., Incropera, F. P, and Dewitt, D. P. *Foundamentals of Heat and Mass Transfer.* John Wiley and Sons, 2011.

[22] Idel'chik, I.E. *Handbook of hydraulic resistance.* Published for the U.S. Atomic Energy Commission and the National Science Foundation, Washington, D.C. by the Israel Program for Scientific Translations, 1966.

[23] Ostanek, K. J. "Improving pin-fin heat transfer predictions using artificial neural network." *ASME Journal of Turbomachinery*, 136: 1–9, 2014.

[24] VanFossen, J. G. "Heat-transfer coefficients for staggered arrays of short pin fins." *ASME Journal of Engineering and Power*, 104: 268–274, 1982.

[25] Metzger, D., Shepard, W., and Haley, S. "Row resolved heat transfer variations in pin-fin arrays including effects of non-uniform arrays and flow convergence." *ASME Paper*, 86-GT-132, 1986.

[26] Faulkner, E. F. *Analytical Investigation of Chord Size and Cooling Methods on Turbine Blade Cooling Requirements.* NASA CR-120883, 1971.

[27] Armstrong, J. and Winstanley, D. "Review of staggered array pin fin heat transfer for turbine cooling applications." *ASME Journal of Turbomachinery*, 110:94–103, 1988.

[28] Ligrani, P. "Heat transfer augmentation technologies for internal cooling of turbine components of gas turbine engines." *International Journal of Rotating Machinery, Review article*, ID 275653, 2013.

[29] Ligrani, P., Oliveira, M. M., and Blaskovich, T. "Comparison of heat transfer augmentation techniques." *AIAA Journal*, 41(3):337–362, 2003.

[30] Gupta, S, Chaube, A., and Verma, P. "Review on heat transfer augmentation techniques: Application in gas turbine blade internal cooling." *Journal of Engineering Science and Technology, Review article*, 05:52–57, 2012.

[31] Hyung Hee Cho, Kyung Min Kim and Song, Jiwoon. *Cooling Systems: Energy, Engineering and Applications - Application of impingement jet cooling systems blade internal cooling.* Published for the U.S. Atomic Energy Commission and the National Science Foundation, Washington, D.C. by the Israel Program for Scientific Translations, 2011.

[32] Martin, H. "Heat and mass transfer between impinging gas jets and solid surfaces." *Advances in Heat Transfer*, 13:01–60, 1977.

[33] Gardon, Robert and Akfirat, J. Cahit. "Heat transfer characteristics of impinging twodimensional air jets." *Journal of Heat Transfer*, 88: 101–108, 1966.

[34] Bradbury, L. J. S. "The structure of a self-preserving turbulent plane jet." *Journal of Fluid Mechanics*, 23:31–64, 1965.

[35] Sparrow, E. M. and Wong, T. C. "Impingement heat transfer coefficients due to initially laminar slot jets." *International Journal of Heat and Mass Transfer*, 18:597–605, 1975.

[36] Goldstein, R. J. "Film cooling." *Advances in Heat Transfer*, 7: 357–358.

[37] Goldstein, R. J. and Seol, W. S. "Heat transfer to a row of impinging circular air jets including the effect of entrainment." *International Journal of Heat and Mass Transfer*, 34:2133–2147, 1991.

[38] Goldstein, R. J. and Behbahani, A. I. "Impingement of a circular jet with and without cross flow." *International Journal of Heat and Mass Transfer*, 225:1377–1382, 1982.

[39] Florschuetz, L., Truman, C., and Metzger, D. "Streamwise flow and heat transfer distributions for jet array impingement with crossflow." *ASME Journal of Heat Transfer*, 103:337–342, 1981.

[40] Kercher, D M. and Tabakoff, W. "Heat transfer by a square array of round jets impinging perpendicular to a flat surface including the effect of spent air." *Journal of Engineering for Power*, 92:73–82, 1970.

[41] Bailey, J C. and Bunker, R S. "Local heat transfer and flow distributions for impinging jet arrays of dense and sparse extent." *ASME Paper*, GT2002-30473, 2002.

[42] Bunker, R S., Dees, J E., and Palafox, P. *Impingement cooling in gas turbines: Design, applications, and limitations - Impingement Jet Cooling in Gas Turbines.* WITpress, Editors: Ryoichi S. Amano & Bengt Sundén, 2014.

[43] Facchini, B, Surace, M., and Tarchi, L. "Impingement cooling for modern combustors: experimental analysis and preliminary design." *ASME Paper*, GT2005-68361, 2005.

[44] Matsumoto, R., Ishihara, I., Yabe, T., Ikeda, K., Kikkawa, S., and Senda, M. "Impingement heat transfer within arrays of circular jets including the effect of crossflow." *Proceedings of ASME/JSME Joint Thermal Engineering Conference*, AJTE99-6386, 1999.

[45] Bogard, D. *The Gas Turbine Handbook - Airfoil Film Cooling.* NETL.

[46] Bonini, A. *A Decoupled Conjugate Heat Transfer Procedure Involving Flow Network Approach: application to GT blade cooling.* PhD thesis, Università degli Studi di Firenze, Dipartimento di Energetica Sergio Stecco, 2011.

[47] Bunker, R. S. "A review of shaped hole turbine film-cooling technology." *ASME Journal of Heat Transfer*, 127:441–453, 2005.

[48] 7-7-7 shaped hole description, 2015. URL `http://www.mne.psu.edu/psuturbine/PublicShapedHole.html`.

[49] L'Ecuyer, M. R. and Soechting, F. O. "A model for correlating flat plate film-cooling effectiveness for rows of round holes." *AGARD Paper*, CP-390, 1985.

[50] Baldauf, S., Scheurlen, M., Schulz, A., and Wittig, S. "Correlation of film-cooling effectiveness from thermographic measurements at enginelike conditions." *ASME Journal of Turbomachinery*, 124: 686–698, 2002.

[51] Goldstein, R. J. "Film cooling." *Advances in Heat Transfer*, 7: 321–379, 1971.

[52] Colban, W. F., Thole, K. A., and Bogard, D. "A film-cooling correlation for shaped holes on a flat-plate surface." *ASME Journal of Turbomachinery*, 133(1):011002/01–011002/11, 2011.

[53] Seller, J. P. "Gaseous film cooling with multiple injection stations." *AIAA Journal*, 1:2154–2156, 1963.

[54] Harrington, M., McWaters, M., Lemmon, C. A., and Thole, K. A. "Full-coverage film cooling with short normal injection holes." *ASME Journal of Turbomachinery*, (123):798–805, 2001.

[55] Ceccherini, A., Facchini, B., Tarchi, L., and Toni, L. "Combined effect of slot injection, effusion array and dilution hole on the cooling performance of a real combustor liner." *ASME Paper*, GT2009-60047, 2009.

[56] Kirollos, B. and Povey, T. "An energy-based method for predicting the additive effect of multiple film cooling rows." *ASME Paper*, GT2013-94934, 2013.

[57] Brown, S. E. "21st century hot engines." *Popular Science*, pages 83–89, 1990.

[58] Sweeney, P. C. and Rhodes, J. F. "An infrared technique for evaluating turbine airfoil cooling designs." *Journal of Turbomachinery*, 122:171–177, 2000.

[59] Annerfeldt, M. O., Persson, J. L., and Torisson, T. "Experimental investigation of impingement cooling with turbulators or surface enlarging elements." *ASME Paper*, 2001-GT-0149, 2001.

[60] Liu, Y., Song, S., and Lo, Y. "Jet impingement heat transfer on target surfaces with longitudinal and transverse grooves." *International Journal of Heat and Mass Transfer*, 58:292–299, 2013.

[61] Mhetras, S., Han, J. C., and Huth, M. "Impingement heat transfer from jet arrays on turbulated target walls at large reynolds numbers." *Journal of Thermal Science and Engineering Applications*, 6: 021003/1–021003/10, 2014.

[62] Kanokjaruvijit, K. and Martinez-Botas, R. F. "Heat transfer and pressure investigation of dimple impingement." *ASME Paper*, GT2005-68823, 2005.

[63] Lutade, P. V., Khanwalkar, P. M., and Kore, S. S. "Heat transfer enhancement by jet impingement on dimpled surface with different cavities." *International Journal of Engineering and Innovative Technology*, 4(5):152–155, 2014.

[64] Rao, Y., Wan, C., Xu, Y., and Zang, S. "Local heat transfer characteristics in channels with pin fin and pin fin-dimple arrays." *ASME Paper*, GT2011-45449, 2011.

[65] Rao, Y., Wan, C., Xu, Y., and Zang, S. "An experimental and numerical study of flow and heat transfer in channels with pin fin-dimple combined arrays of different configurations." *Journal of Heat Transfer*, 134(12):12190/1–12190/11, 2012.

[66] Simpson, T. W. "AM need MEs." *ASME Mechanical Engineering*, 137:30–35, 2015.

[67] Snyder, J. C., Stimpson, C. K., Thole, K. A., and Mongillo, D. "Build direction effects on additively manufactured channels." *ASME Paper*, GT2015-43935, 2015.

[68] Stimpson, C. K., Snyder, J. C., Thole, K. A., and Mongillo, D. "Roughness effects on flow and heat transfer for additively manufactured channels." *ASME Paper*, GT2015-43940, 2015.

[69] Zhenfeng, W., Hongyan, H., Peigang, Y., and Wanjin, H. "Coupled BEM and FDM conjugate analysis of a three-dimensional air-cooled turbine vane." *ASME Paper*, GT2009-59030, 2009.

[70] Facchini, B., Magi, A., and Scotti Del Greco, A. "Conjugate heat transfer simulation of a radially cooled gas turbine vane." *ASME Turbo Expo*, GT2004-54213, 2004.

[71] Luo, J. and Razinsky, E. H. "Conjugate heat transfer analysis of a cooled turbine vane using the v2f turbulence model." *Journal of Turbomachinery,*, 129:773–781, 2007.

[72] Bohn, D., Bonhoff, B., Schönenborn, H., and Wilhelmi, H. "Validation of a numerical model for the coupled simulation of fluid flow and diabatic walls with application to film-cooled gas turbine blades." *VDI-Berichte*, 1186:259–272, 1995.

[73] Bohn, D., Bonhoff, B., and Schönenborn, H. "Combined aerodynamic and thermal analysis of a high-pressure turbine nozzle guide vane." *Proceedings of IGTC*, 108:I–35–I–39, 1995.

[74] Takahashi, T., Watanabe, K., Takahashi, T., and Wilhelmi, H. "Thermal conjugate analysis of a first stage blade in a gas turbine." *ASME Paper*, GT2000-0251, 2000.

[75] Kassab, A., Divo, E., Heidmann, J., Steinthorsson, E., and Rodriguez, F. "BEM/FVM conjugate heat transfer analysis of a three-dimensional film cooled turbine blade." *International Journal of Numerical Methods for Heat & Fluid Flow*, 13(5):581–610, 2003.

[76] Kassab, A., Divo, E., Heidmann, J., Steinthorsson, E., and Rodriguez, F. "Conjugate Heat Transfer Effects on a Realistic Film Cooled Turbine Vane." *ASME Paper*, (GT2003-38553), 2003.

[77] Han, J. C., Ortman, D.W., and Lee, C.P. "A Computer Model for Gas Turbine Blade Cooling Analysis." *ASME Paper*, 82-JPGC-GT-6, 1982.

[78] Jelisavcic, N., Moral, R. J., Dulikravich, G. S., Martin, T. J., Sahoo, D., and Gonzalez, M. "Design optimization of networks of cooling passages." *Proceedings of ASME IMECE*, IMECE2005-79175, 2005.

[79] Martin, T. J. and Dulikravich, G. S. "Analysis and multidisciplinary optimization of internal coolant networks in turbine blades." *Journal of Propulsion and Power*, 18(4):896–906, 2002.

[80] Carcasci, C., Facchini, B., and Ferrara, G. "A rotor blade cooling design method for heavy duty gas turbine applications." *Proceedings of ASME Cogenturbo Power Conference*, 95-CTP-90, 1995.

[81] Carcasci, C. and Facchini, B. "A numerical procedure to design internal cooling of gas turbine stator blades." *Revue Générale de Thermique*, 35:257–268, 1996.

[82] Arnone, A., Liou, M. S., and Povinelli, L. A. "Navier-Stokes solution of transonic cascade flow using non-periodic C-type grids." *Journal of Propulsion and Power*, 8(2):410–417, 1992.

[83] Zecchi, S., Arcangeli, L., Facchini, B., and Coutandin, D. "Features of a Cooling System Simulation Tool Used in Industrial Preliminary Design Stage." *ASME Paper*, GT2004-53547, 2004.

[84] Hylton, L. D., Mihelc, M. S., Turner, E. R., Nealy, D. A., and York, R. E. "Analytical and experimental evaluation of the heat transfer distribution over the surfaces of turbine vanes." *NASA Contractor Report*, NASA CR-168015, 1983.

[85] Kumar, B.V.N.R. and Prasad, B.V.S.S.S. "A combined CFD and network approach for a simulated turbine blade cooling system." *Indian Journal of Engineering and Materials Science*, 13:195–201, 2006.

[86] Alizadeh, M., Izadi, A., and Fathi, A. "Sensitivity analysis on turbine blade temperature distribution using conjugate heat transfer simulation." *Journal of Turbomachinery*, 136(1):011001/1–011001/13, 2014.

[87] Chowdhury, N. H. K., Zirakzadeh, H., and Han, J. C. "A predictive model for preliminary gas turbine blade cooling analysis." *ASME Paper*, GT2015-42205, 2015.

[88] E., Halila E., T., Lenahan D., and T., Thomas T. "High pressure turbine test hardware detailed design report." *NASA Contractor Report*, 1982.

[89] Arnone, A., Marconcini, M., and A. Scotti Del Greco, E. Spano. "Numerical investigation of three-dimensional clocking effects in a low pressure turbine." *Journal of Turbomachinery*, 126:375–384, 2004.

[90] Povey, T., Chana, K. S., Jones, T. V., and Hurrion, J. "The effect of hot-streaks on hp vane surface and endwall heat transfer: An experimental and numerical study." *Journal of Turbomachinery*, 129:32–43, 2007.

[91] L. Zhang, J. Yin and Moon, H. K. "The effects of vane showerhead injection angle and film compound angle on nozzle endwall cooling (phantom cooling)." *ASME Paper*, GT2014-25289, 2014.

[92] Maffulli, R. and L.He. "Wall temperature effects on heat transfer coefficient." *ASME Paper*, (GT2013-94291), 2013.

[93] Maffulli, R. and L.He. "Dependence of external heat transfer coefficient and aerodynamics on wall temperature for 3-D turbine blade passage." *ASME Paper*, (GT2014-26763), 2014.

[94] B. Morini, M. Porcelli. "TRESNEI, a Matlab trust-region solver for systems of nonlinear equalities and inequalities." *Computational optimization and applications*, 51:27–49, 2012.

[95] M. Gritsch, S. Wittig A. Schulz. "Effect of crossflows on the discharge coefficient of film cooling holes with varying angles of inclination and orientation." *Journal of Turbomachinery*, 123(4):781–787, 2001.

[96] A. W. Reichert, D. Brillert and Simon, H. "Loss prediction for rotating passages in secondary air systems." *ASME Paper*, (GT-215), 1997.

[97] R. Da Soghe, A. Andreini. "Numerical characterization of pressure drop across the manifold of turbine casing cooling system." *Journal of Turbomachinery*, 135(3):031017/1–031017/9, 2013.

[98] J. Ling, J. K. Eaton R. Rossi. "Near wall modeling for trailing edge slot film cooling." *Journal of Fluids Engineering*, 137(2): 021103/1–021103/10, 2015.

[99] Ansys, Inc. *Mechanical APDL User's Guide*. 2014.

[100] York, W. D. and Leylek, J. H. "Three-dimensional conjugate heat transfer simulation of an internally-cooled gas turbine vane." *ASME Paper*, GT2003-38551, 2003.

[101] Ledezma, A. G., Laskowski, G. M., and Tolpadi, A. K. "Turbulence model assessment for conjugate heat transfer in a high pressure turbine vane model." *ASME Paper*.

[102] Rohsenow, M. W., Hartnett, J. P., and Cho, Y. I. *Handbook of Heat Transfer*. McGraw-Hill Handbooks, 1998.

[103] Menter, F. R. "Two-equation eddy-viscosity turbulence models for engineering applications." *AIAA Journal*, 32(8):1598–1605, 1994.

[104] Hylton, L. D., Nirmalan, N. V., Sultanian, B. K., and Kaufman, R. M. "The effects of leading edge and downstream film cooling on turbine vane heat transfer." *NASA Contractor Report*, NASA CR-182133, 1988.

[105] Garg, V. K. and Gaugler, R. E. "Effect of velocity and temperature distributionat the hole exit on film cooling of turbine blades." *Journal of Turbomachinery*, 119:347–351, 1997.

[106] Hall, E. J., Topp, D. A., Delaney, R. A., Walker, G. J., Hodson, H. P., and Shin, H.W. "Aerodynamic/heat transfer analysis of discrete site film-cooled turbine airfoils." *AIAA Paper*, 94-3070, 1994.

[107] Sarkar, S., Das, K., and Basu, D. "Two-dimensional Navier-Stokes analysis of an internally cooled turbine blade." *Journal of Power and Energy*, 214(A):585–598, 2000.

[108] Mangani, L., Cerutti, M., Maritano, M., and Spel, M. "Conjugate heat transfer analysis of NASA C3X film cooled vane with an object-oriented CFD code." *ASME Paper*, GT2010-23458, 2010.

[109] Garg, V. K. and Gaugler, R. E. "Leading edge film cooling effects on turbine blade heat transfer." *NASA Technical Memorandum*, NASA TM-106955, 1995.

[110] Sarkar, S., Das, K., and Basu, D. "Film cooling on a turbine guide vane: a numerical analysis with a multigrid technique." *Journal of Power and Energy*, 215(A):39–53, 2001.

[111] Facchini, B, Surace, M., and Zecchi, S. "A new concept of impingement cooling for gas turbine hot parts and its influence on plant performance." *ASME Paper*, GT2003-38166, 2003.

[112] Tarchi, L., Cocchi, L., Facchini, B., Winchler, L., Innocenti, L., Andrei, L., and Bonini, A. "Experimental investigation on impingement array cooling systems through IR thermography - Paper accepted for conference." *ASME Paper*, (GT2016-57436), 2016.

[113] Conti, S. "Development of an innovative film cooling shaped hole by means of CFD optimization." *MS thesis, Universitá degli studi di Firenze, Department of Industrial Engineering of Florence (DIEF)*, 2015.

[114] Sinha, A. K., Bogard, D. G., and Crawford, M. E. "Film cooling effectiveness downstream of a single row of holes with variable density ratio." *Journal of Turbomachinery*, 113:442–449, 1991.

[115] Pietrzyk, J. R. *Experimental study of the interaction of dense jets with a crossflow for gas turbine applications.* PhD thesis, University of Texas, Austin, 1989.

[116] Ansys, Inc. *DesignXplorer User's Guide.* 2014.

[117] Jones, T. V. "Theory for the use of foreign gas in simulating film cooling." *International Journal of Heat and Fluid Flow*, 20:349–354, 1999.

[118] Navarra, K. R. "Development of the pressure-sensitive-paint technique for turbomachinery applications." *MS thesis, Virginia Polytechnic Institute and State University*, 1997.

[119] Caciolli, G., Facchini, B., Picchi, A., and Tarchi, L. "Comparison between psp and tlc steady state techniques for adiabatic effectiveness measurement on a multiperforated plate." *Experimental Thermal and Fluid Science*, 48:122–133, 2013.

[120] Andreini, A., Becchi, R., Facchini, B., Mazzei, L., Picchi, A., and Turrini, F. "Adiabatic effectiveness and flow field measurements in a realistic effusion cooled lean burn combustor." *ASME Paper*, (GT2016-42584), 2015.

[121] Singh, R. "Process capability study of polyjet printing for plastic components." *Journal of Mechanical Science and Technology*, 25(4): 1011–1015, 2011.

[122] VERODENT MED670 material datasheet, 2015. URL `http://www.stratasys.com/it/materiali/material-safety-data-sheets/polyjet/dental-and-bio-compatible-materials`.

[123] Andrei, L. *Film Cooling Modelling for Gas Turbine Nozzles and Blades: Validation and Application.* PhD thesis, Universitá degli studi di Firenze, Department of Industrial Engineering of Florence (DIEF), 2013.

[124] Kumar, K. and Kumar, G. S. "An experimental and theoretical investigation of surface roughness of poly-jet printed parts." *Virtual and Physical Prototyping*, 10(1):23–34, 2015.

[125] Xml parser for fortran, 2015. URL `http://xml-fortran.sourceforge.net/`.